

**EXPERIMENTAL STUDY ON STATIC AND DYNAMIC
BEHAVIOR OF WOVEN CARBON FABRIC LAMINATES
USING IN-HOUSE PIEZOELECTRIC SENSORS, ACOUSTIC
EMISSION, DIGITAL IMAGE CORRELATION AND
SCANNING ELECTRON MICROSCOPY**

By

Hafiz Qasim Ali

Submitted to the Graduate School of Engineering and Natural Sciences
in partial fulfillment of
the requirements for the degree of
Master of Science

SABANCI UNIVERSITY

July 2019

EXPERIMENTAL STUDY ON STATIC AND DYNAMIC BEHAVIOR OF WOVEN CARBON FABRIC LAMINATES USING IN-HOUSE PIEZOELECTRIC SENSORS, ACOUSTIC EMISSION, DIGITAL IMAGE CORRELATION AND SCANNING ELECTRON MICROSCOPY

APPROVED BY

Professor Mehmet Yildiz
(Thesis supervisor)



Assistant professor. Eralp Demir



Assistant professor. Bertan Beylergil



Date of approval: 09/07/2019 _____

© Hafiz Qasim Ali 2019
All Rights Reserved

EXPERIMENTAL STUDY ON STATIC AND DYNAMIC BEHAVIOR OF WOVEN
CARBON FABRIC LAMINATES USING IN-HOUSE PIEZOELECTRIC SENSORS,
ACOUSTIC EMISSION, DIGITAL IMAGE CORRELATION AND SCANNING ELECTRON
MICROSCOPY

Hafiz Qasim Ali

MSc. Dissertation, July 2019

Thesis supervisor: Prof. Dr. Mehmet Yildiz

ABSTRACT

Keywords: Piezopolymer, Piezoelectric sensor, Nanofibers, Fatigue analysis, Acoustic Emission, Cluster evaluation, Digital Image Correlation, Fractography

This study focuses on dynamic and static failure analysis of carbon fabric reinforced polymeric composite materials. The first part signifies the production of Piezoelectric Polyvinylidene fluoride (PVDF) nanofibers-based sensor for structural health monitoring of composites. Results obtained from the characterization of electrospun PVDF nanofibers confirm that electrospinning promotes the formation of β -phase. Dynamic flexural tests are performed on woven carbon fabric composites with embedded and surface mounted PVDF sensors to study the capability of these sensors to record strain history and damage progression in composite materials. Moreover, these PVDF sensors are able to capture three distinct stages of fatigue life of composite specimen. This result is validated by the strain measurement with the video extensometer during tests. It is important to emphasize that surface mounted PVDF sensors do not show any sign of malfunctioning during the test. SEM analysis of fractured surfaces of composite specimens shows vivid delamination and fiber pullouts through the thickness, thus indicating gradual growth of damage in laminates. The second part of this study is related to static failure analysis of woven fabric carbon reinforced polymeric composites under tensile and flexural loading. To conduct a detailed investigation Acoustic Emission (AE) is used to attain damage evolution under flexural loading conditions. For the first time *GAP* function has been suggested to find out the optimal number of clusters for AE data, the advantage of this function is its suitability for classifying elongated data points in vectoral space of acoustic data. Three clusters of data are determined with this new approach indicating various failure types in composite laminates and it is shown that simultaneous occurrence of all failures results in a major change of material stiffness. These failures are also substantiated by Scanning Electron Microscope (SEM) studies of fracture surfaces. Further studies on tensile behavior of the same laminates are conducted with the help of SEM micrographs and 3D-digital image correlation (DIC) technique. Remarkably, it is seen that presence of the shear and transverse strain fields at the surface of the tensile specimen obtained through DIC technique can be correlated to shear dominant and high energy failure (interlaminar delamination and fiber pull outs) respectively, which are also confirmed by SEM images of same fracture regions.

DOKUMA KARBON KUMAŞ LAMİNATLARIN STATİK VE DİNAMİK
DAVRANIŞLARININ DENEYSEL OLARAK ŞAHSİ ÜRETİM PİEZOELEKTRİK SENSÖR,
AKUSTİK EMİSYON, DİJİTAL GÖRÜNTÜ KORELASYONU VE TARAMALI ELEKTRON
MİKROSKOBU İLE İNCELENMESİ

Hafız Qasim Ali

Yüksek Lisans Tezi, Temmuz 2019

Tez Danışmanı: Prof. Dr. Mehmet Yıldız

Anahtar Kelimeler: Piezopolimer, Piezoelektrik sensör, Nanofiberler, Yorulma Analizi, Akustik Emisyon, Kümelenme, Dijital Görüntü Korelasyonu, Fraktografi

Özet

Bu çalışma, karbon kumaş takviyeli polimerik kompozit malzemelerin dinamik ve statik hasar analizine odaklanmaktadır. İlk bölümde, kompozitlerin yapısal sağlık izlemesi için Piezoelektrik Poliviniliden Florür (PVDF) nano fiber bazlı sensörün üretimine vurgu yapılmaktadır. Elektropsun PVDF nano elyaflarının karakterizasyonundan elde edilen sonuçlar, elektropsinlamanın β -faz oluşumunu desteklediğini doğrulamaktadır. Bu sensörlerin gerinim geçmişi kaydetme ve kompozit malzemelerde hasar ilerlemesi ölçme yeteneğini incelemek için, gömülü ve yüzeye monte PVDF sensörleri ile dokunmuş karbon kumaş kompozitler üzerinde dinamik eğilme testleri yapılmıştır. Ayrıca, PVDF sensörleri kompozit numunenin yorulma ömrünün üç farklı aşamasını yakalayabilmektedir. Bu sonuç, testler sırasında video ekstansiyometre ile gerinim ölçümü yapılarak doğrulanmıştır. Yüzeye monte PVDF sensörlerinin test sırasında herhangi bir arıza belirtisi göstermediği gözlemlenmiştir. Kompozit numunelerin hasara uğramış yüzeylerinin Taramalı Elektron Mikroskobu (SEM) analizi, numunenin kalınlığı boyunca belirgin delaminasyon ve fiber kesilmelerini göstermiştir. Bu şekilde laminatlarda hasarın kademeli olarak büyüdüğü gözlemlenmiştir. Bu çalışmanın ikinci kısmı, dokuma kumaş karbon takviyeli polimerik kompozitlerin çekme ve eğilme yüklemesi altında statik hasar analizi ile ilgilidir. Eğilme yükü koşullarında hasar oluşumunu detaylı olarak gözlemlmek için Akustik Emisyon (AE) ölçüm methodu kullanılmıştır. İlk kez GAP fonksiyonunun akustik emisyon verileri için en uygun küme sayısını bulduğu tespit edilmiştir ve bu metodun en büyük avantajı, uzun akustik veri alanlarındaki çoklu veri noktalarının sınıflandırılmasında uygunluğudur. Kompozit laminatlardaki çeşitli hasar tiplerini tespit eden bu yeni yaklaşımla üç hasar veri kümesi belirlenir ve tüm hasarların eşzamanlı olarak ortaya çıkmasının, önemli bir malzeme rijitliği değişikliği ile sonuçlandığı gözlemlenmiştir. Bu hasarlar ayrıca kırılma yüzeylerinin Taramalı Elektron Mikroskobu (SEM) çalışmaları ile de kanıtlanmaktadır. Aynı laminatların gerilme davranışı ile ilgili diğer çalışmalar, SEM mikrografları ve 3D-dijital görüntü korelasyonu (DIC) tekniği ile gerçekleştirilmiştir. Dikkat çekici bir şekilde, DIC tekniği ile elde edilen gerilme numunesinin yüzeyinde kayma ve enine gerinim alanlarının varlığının aynı kırılma bölgelerinin SEM görüntüleri ile de teyit edilen, sırasıyla kayma ve yüksek enerjili hasar (interlaminar delaminasyon ve lif çikintıları) ile ilişkili olabileceği görülmektedir.

Acknowledgement

At first, I would like to thank to Higher Education Commission (HEC) Pakistan for their financial support and providing me the opportunity to conduct my research at Sabanci university which is one of the most prestigious institute in Turkey. After that I would like to express my gratitude to my thesis advisor professor Mehmet Yildiz for his continuous support throughout my studies and research work. I sincerely think that I would not be able to complete my MSc. degree without his assistance.

Next, I want to acknowledge Dr. Jamal Seyyed Monfared Zanjani who proposed me the idea for my thesis work and supported me in every aspect whether it was experimental or theoretical. I am also grateful to Dr. Çagatay Yilmaz, Mr. Isa Emami, Mr. Gokhan Inan and Mr. Raja Awais for their guidance and motivation, without them this work would never be possible. I also want to thank Mr. Fatih Uzun and Mr. Faisal Jamil for their support in all the difficult situations I had face here due to the cultural and language barrier. Special thanks to Mrs. Serra Topal, Mr. Murat Isik, Mr. Pouya Yousefi and Mr. Francisco for their motivation and help at the ultimate stages of my thesis.

At last, I would like to express deepest appreciation to all the engineers and employers of SUIMC for their help to conduct this research work, it was almost impossible to complete this work without their assistance. I am confident that this center will progress by leaps and bound because of untiring hard work of this competitive team.

Table of Contents

ABSTRACT	iv
Özet	v
Acknowledgement	vi
CHAPTER 1	1
1. Introduction	1
CHAPTER 2	8
2. Literature review	8
2.1. Scope	8
2.2. Piezoelectricity	9
2.3. Piezoelectric polymers	10
2.4. Polyvinylidene Fluoride	11
2.5. Fatigue Testing	16
2.6. Digital Image Correlation (DIC)	19
2.7. Acoustic emission (AE)	23
2.8. Scanning Electron Microscopy (SEM)	30
CHAPTER 3	31
3. Dynamic analysis of composites	31
3.1. Summary	31
3.2. Experimental	31
3.3. Results and Discussions	34
CHAPTER 4	49
4. Static failure of composite materials	49
4.1. Summary	49
4.2. Experimental	49
4.3. Results and Discussions	50
CHAPTER 5	62
5. Conclusion	62
References	64

List of Figures

Figure 1 Vinylidene fluoride polymerization.....	11
Figure 2. Different phases of PVDF[68].....	12
Figure 3 Random and aligned orientation of dipoles of PVDF β -phase	13
Figure 4. Phase transformation process of PVDF [71].	14
Figure 5. Phase transformation of PVDF due to stretching	15
Figure 6. S-N curve depicting the effect of different stress level on the life of a material [75].....	17
Figure 7 Standard terms for cyclic amplitude loading [75]	18
Figure 8. Loading types [76].....	19
Figure 9. Schematic of DIC measurement system [79]	21
Figure 10. Facet size	22
Figure 11 Increment in facet step.....	22
Figure 12. Base calculation.....	23
Figure 13. Schematic of acoustic emission testing [84].....	25
Figure 14. Acoustic emission hit based features [88].	27
Figure 15. The schematic representation of the electrospinning setup for PVDF nanofibers.....	32
Figure 16. Schematic representation of fatigue testing, testing setup, and specimens.....	34
Figure 17. FTIR spectrum of PVDF nanofibers and PVDF granule.....	35
Figure 18. DSC curves of PVDF granule and nanofibers.	37
Figure 19. XRD spectrum of PVDF nanofibers and PVDF granule.....	38
Figure 20. SEM images of PVDF nanofibers.	39
Figure 21. The variation of strain difference between peak and trough values as a function of the fatigue cycle for S1 and S2 specimens.....	40
Figure 22. Measured voltage and strain against the number of cycles for S1.....	41
Figure 23. Fatigue evaluation of sample S2: (a) Strain vs time. (b) FFT spectrum of strain vs No. of cycles. (c) Strain vs No. of cycles.....	42
Figure 24. Piezoelectric response of PVDF sensor: (a) Voltage vs time. (b) FFT of voltage vs No. of cycles. (c) Voltage vs Cycles.....	44
Figure 25. (a) Trend of voltage vs strain, (b) Slope of voltage vs strain plot.	44
Figure 26. The variation of maximum strain recorded by extensometer and PVDF sensor as a function of the fatigue cycle.	45
Figure 27. (a-d) Micrographs of fatigue failure for S1 and S2 where subfigures a is taken parallel to fracture surface along the width direction while the rest of the images are taken from the fracture surface.	47
Figure 28. SEM micrographs of carbon fibers from failure regions of composites. (a) & (b) rupture dominant region; (c) & (d) shear dominant region.	51
Figure 29. Failure of composites (a) broken sample; (b) & (c) strain map of ϵ_{yy} , ϵ_{xy} ; (d) & (e) SEM images of fractured surfaces of the composite.....	55
Figure 30. (a) Acoustic emission results for flexural test; (b) Gap values obtained for each cluster numbers.....	57
Figure 31. Clustering results for specimen under flexural loading.	58
Figure 32. Flexural strength and energy versus strain and time for a) B1 b) B2	60
Figure 33. SEM images of fractured surfaces of the composite under three-point bend loading	61

List of Tables

Table 1. Comparison of the properties of smart materials.	10
Table 2. Piezoelectric constants of smart materials.....	10
Table 3. Properties of PVDF.....	16
Table 4. Important parameters for fatigue testing	17
Table 5. Tensile and Three-point results.	51
Table 6. Frequency ranges	56

List of Equations

$x^* = x + u + \partial u \partial x \Delta x + \partial u \partial y \Delta y$	Equation 2	20
$y^* = y + v + \partial v \partial x \Delta x + \partial v \partial y \Delta y$	Equation 3	20
$F\beta = A\beta K\beta / K\alpha A\alpha + A\beta \times 100$	Equation 4	35
$C\% = \Delta H_i / \Delta H_m \times 100$	Equation 5	36
$f_{Centroid} = s = 0s = 1000 f_s M(s) s = 0s = 1000 M(s)$	Equation 6	56
$Weighted\ Peak\ frequency\ (WPF) = f_{Centroid} \times f_{peak}$	Equation 7	56
$GAP_{nk} = E_n * \log w_k - \log(w_k)$	Equation 8	56

CHAPTER 1

1. Introduction

Piezoelectric materials are the smart materials which are commonly used as energy harvesting devices or sensors [1]. The main property of these materials is the ability to accumulate electrical charge when subjected to external mechanical load [2]. Piezoelectric materials can either be ceramic or polymer-based depending on their rigidity and crystal structure. A compelling type of polymer-based piezoelectric material is Polyvinylidene fluoride (PVDF) which can directly convert mechanical energy to electrical voltage, thus lending itself to a wide range of applications in engineering structures in the form of sensors, actuators, and energy harvesters [3].

PVDF is a thermoplastic polymer with a semi-crystalline nature. Among all polymeric piezoelectric materials, PVDF has a better piezoelectric response due to its crystal structure [4]. It has four crystalline phases namely α , β , γ , and δ in which the first two phases are considered as the low-temperature stable structures of PVDF materials. Thermodynamically, α -phase is the most stable state and it is formed through melting and solution casting [5]. In this phase, chains are arranged in Trans-Gauche Trans-Gauche (TG^+TG^-) conformation; thus, the net dipole moment will be zero because of the antiparallel arrangement of fluoride atoms along with carbon atoms at backbone chain. As a consequence, no piezoelectric effect can be observed for this configuration [6]. On the other hand, β -phase is an electro active-phase which shows piezoelectric response because of all dipolar moments in its structure point in the same direction. The β -phase contains all Trans (TTTT) formations where all the chains are arranged parallel to the b-axis and dipoles form a non-centrosymmetric crystal structure with high piezoelectric capability [7]. The γ -phase has a TTTG formation in which molecular chains are packed in a parallel non-centrosymmetric polar unit crystal [8]. The δ -phase resembles with the α -phase in terms of their polarity and the unit cell dimensions but a cell pack contains two chains so that their dipoles strengthen each other [9]. β -phase is the main crystal structure favored for applications as sensor and energy harvesting devices due to its stable piezoelectric nature.

Several methods are introduced in the literature for the manufacturing of PVDF polymers such as melt casting, stretching, solvent casting and copolymerization [10]. The stretching process promotes the formation of electroactive phase, i.e. β -phase. This polling process consists of

mechanical stretching and electrical poling to fabricate piezoelectric material. One way of conducting the stretching process is the electrospinning method, in which a polymer solution is spun under the influence of the strong electrical field [11]. This method produces dry fibers with diameters ranging from a few nanometers to a few micrometers depending on electrospinning operational parameters used [12]. Fang et al. electrospun randomly oriented PVDF fibers used as an active layer for energy conversion. In their FTIR spectrum of as-spun nanofibers shows a strong peak at 840 cm^{-1} which is a characteristic peak for β -crystalline phase while XRD analysis exhibits a crystalline signal at $2\theta=20.5^\circ$ [13]. Sengupta et al. reported that high voltage for the electrospinning of PVDF fibers is favorable as it promotes the formation of β -phase [14]. The thin films of β -phase produced through electrospinning procedure can be used for versatile structural health monitoring (SHM) purposes.

Various sensors based on different working principals have been utilized for SHM purposes [15–17]. For example, Akay et al. monitored the degradation of Poisson's ratio through embedded FBG (Fiber bragg grating) sensors under fatigue loading [18]. The aptness of FBG sensors is manifested; however, the requirement for an external source of light is considered a major drawback. Moreover, several investigations have focused on SHM using piezoelectric sensors. Shin et al. reported the response of commercially purchased PVDF film by mounting it on a Polyamide specimen subjected to tension-compression fatigue test up to 10^7 cycles. PVDF film showed a stable response and did not get damaged due to the cyclic loading [19]. Hofmann et al. studied the impact and bending response of piezoelectric fabric-based fiber reinforced plastic. In the bending test, the amplitude of the sensor's signal increases as the test proceeds and specimen undergoes higher load which makes reinforcer to be acted as a sensor for structural health monitoring [20]. Zhang et al. employed surface-mounted piezoelectric paint sensors to detect surface fatigue crack and suggested that to obtain reliable information from sensors, cracks inside material should cross through the electrodes of the sensor [21]. Gama et al. utilized PVDF sensors to assess the fatigue life of a compact-tension steel specimen, and their results revealed that these sensors could be used successfully instead of conventional resistive strain gauges [22]. However, to increase the accuracy of the obtained data, they had to perform a normalization procedure. De et al. considered PVDF sensors for SHM of aluminum panels and observed that PVDF sensors have voltage responses with high signal to noise ratio thereby being a good alternative to resistive strain gauges [23].

et al. employed built-in piezoceramic sensors to obtain crack growth size index for metallic structures under fatigue loading [24].

Structural health monitoring becomes even more important for composite materials as these materials must maintain a balance between lightweight and excellent mechanical properties and show reliable performance during the service life [25]. Therefore, the prediction of failure and structural health monitoring of composites is an important concern. Despite the capabilities of piezoelectric materials, there have been very few studies performed to assess the applicability of piezoelectric sensors as a structural health monitoring system in fiber reinforced laminates. Some studies have been conducted to provide a reliable damage assessment for composites [21, 24, 26–28]. Cristobal et al. used PVDF sensor to predict the integrity of the composite structure which damaged as a result of impact loading[29]. Chrysochoidis et al. characterized the fatigue performance of the glass fiber and AIREX T92.90 based sandwich composite panel with embedded PVDF sensors in three-point bending configuration and obtained satisfactory performance from the sensor against the applied load [30]. This study only considered the strain measurement and did not focus on the damage monitoring of the sandwich panel. It is the best of the author's knowledge that there is no study on fatigue life characterization and damage assessment of carbon fiber reinforced polymeric materials based on an embedded and a surface mounted PVDF piezoelectric sensors.

Failure initiation and progression of composite materials is a complex mechanism which is strenuously understandable. The response of carbon fiber reinforced composites against tension is almost linear and easily predictable, but layer to layer damage progression and modes of failure are not depictable through the stress-strain curve, therefore, additional techniques are required to study damage accumulation in these materials[31, 32]. Acoustic Emission (AE) considers being one of the promising techniques for damage detection in laminated fiber reinforced polymers.

The occurrence of damages inside composite laminates is accompanied by a burst of energy producing acoustic elastic waves [33]. These acoustic emission waves are used to record damage evolution inside composite materials and provide valuable data regarding damage accumulation during failure progress. Since each damage type occurring inside material releases a distinctive waveform, the features of that wave will be unique for that damage type. This exclusivity can be used to identify and perform subsequent clustering (i.e. classifying) of the damages during

mechanical tests. One of these clustering methods with very well-known applicability in acoustic emission analysis is the K-means method. [34], this method is an unsupervised clustering method, i.e. no initial sample data points are available from each cluster of data and a possible number of clusters are unknown. Thus, the determination of an appropriate number of clusters is an important concern in the K-means method to avoid the generation of erroneous clustering results and cause inappropriate identification of damage types. Various methods have been used to find the optimal number of clusters such as Silhouette coefficient, Davies–Bouldin index, elbow methods while more recent statistical approaches have not been used in composite materials research field [34–37]. One of these statistical techniques is *GAP* statistics that uses a comparison between expected values of a null reference distribution of data and within-cluster variation of data for various K values (i.e. the number of clusters) [38]. This method has demonstrated good results when outputs of the K-means clustering algorithm are implemented on it. To the author's knowledge, no study has used this statistical approach for K-means clustering of acoustic emission activity in composite materials.

Understanding of damage evolution inside woven fabric composites becomes more crucial due to the presence of different fiber directions and multiple interfaces between fibers and matrix material. Li et al. have used peak frequency and peak amplitude to define four clusters of damages inside woven glass epoxy laminates, namely matrix cracking, fiber/matrix debonding, delamination and fiber breakage[36]. Gao et al. have conducted acoustic emission analysis to find out the onset of failure during quasi-static tensile tests of woven carbon fabric laminates. Their results suggest that transverse matrix cracking is the first type of damage that happens with delamination which is followed by longitudinal splitting [39]. In an investigation performed by Loutas et al. on damage accumulation in carbon/carbon woven composites, an algorithmic scheme is used for clustering damage types. Their findings demonstrate that matrix cracking occurs severely at the beginning of loading materials and halts just before the global failure of the sample[40]. Despite its merits, acoustic emission analysis does not give any information about the strain fields during deformation of composite laminate, therefore damage analysis must be accompanied by strain measurements to provide a better understanding of fracture modes in composite materials. Global or local strain measurement methods can be used for strain analysis in material, however, due to anisotropy and heterogenous nature of displacement in composite laminates global measurements are more favorable.

One of the convenient global strain measurement techniques used in composite materials research field is Digital Image Correlation (DIC) which is an optical and non-contact measurement tool with low noise sensitivity [41]. This method uses an algorithm to compare consecutive images taken from the surface of the material during deformation and obtain spatial displacement fields accordingly. DIC enables one to monitor the displacement of materials at different time intervals and different locations, especially for heterogeneous materials such as woven fabric composites [42]. Many investigators have used DIC for damage analysis of woven fabrics, some of the recent studies are mentioned hereby. Tang et al. in their study conclude that woven glass fabric laminates have complex fracture modes due to the inherent presence of weft and warp fibers as well as resin packets in between them [43]. Nicoletto et al. conducted full-field strain measurement in a twill weave carbon fiber composites under tensile loading. Their Results obtained from experiments are compared with the finite element model to assess the mesoscopic strain values[44]. In an investigation by Behrad et al. DIC based multiscale analysis is carried out to inspect the in-plane deformation of woven glass fiber reinforced composites subjected to tension. Their findings show that the bulk failure modes as well as tensile response endow to be extremely sensitive to the angle between fiber orientation and the axis of loading[45]. Boufaida et al. compared DIC results with a numerical model for woven glass fabric thermoplastic resin, they showed that ratio of strain values at fiber-rich areas is 1/3 of resin rich areas and highest strains are located at the interface [46]. Rokbi et al. used DIC to measure the crack length during compact tension test of woven fabric specimens, therein showing that crack propagation always started along fibers at inner plies[47]. In these studies, DIC is just used for the analysis of strain fields in woven fabric composites without any attempt to correlate it with the failed region of the specimen. Thus, for the first time, this investigation aims to attribute failure modes in woven fabric composite laminates to strain mapping obtained through the DIC technique. This approach will enlighten the path for determining the susceptible regions of composite structures based on DIC measurements. Scanning electron microscopy (SEM) is one of the ways to avail this purpose through analysis of fracture surfaces.

Mayen et al. elaborately assessed the failure mechanism of the CFRP laminates through electron microscopy, their results reveal that Fibers failed as a consequence of transverse crack propagation have a rough surface due to the significant amount of resin on their surface. Cups, imprint marks and hackles depict crack propagation, delamination, and inter-fiber fracture respectively[48]. Dixit

et al. evaluated the mechanical behavior of 2x2 twill weave carbon fabric based polymeric composites. Their failure study through SEM analysis provided detailed information about various damage types such as fiber pull out, which happened due to tensile failure, and debonding and matrix cracking as a result of three-point bend testing[49]. Greenhalgh et al. utilized fractography as a powerful tool for the failure studies of composite structures. In their study failures that develop under tension, flexure, shear, and compression are related to translaminar class of failures. Their results suggest that fiber fractures under tension exhibit mirror or hackle patterns because of global direction of failure, while fiber failures under compressive loads happen due to micro-buckling, delamination or ply-splitting which leave a radial mark on one side of fiber while chop mark on the other side[50]. An investigation by Kumar et al. on the tensile failure of unidirectional CFRP laminates unveiled chevron lines, longitudinal matrix splitting, radial and chop marks on the broken end of the fibers. [51] To the author's knowledge, no specific study has been focused on correlating micro damages with macro-strain fields observed on the surface of laminates under loading condition.

The thesis is planned in the following form. In the first section of the paper, synthesizing, and manufacturing of the PVDF sensors are described in detail, and then the approach for embedding the sensor inside the manufactured woven fabric laminates through vacuum infusion process is introduced. Material characterization methods to analyze produced the PVDF sensors (i.e., FTIR, DSC, XRD, SEM) and the composite laminates (i.e., flexural and fatigue tests, SEM) are described together with relevant experimental conditions. The next section of the manuscript starts with the discussion of characterization results for electrospun fibers. Mechanical test results are presented and the relationship between voltage and strain values is determined for PVDF sensor. Results of fatigue test are compared based on the strain values from PVDF sensors and via video extensometer. Reliability of the sensors is demonstrated, and three distinct stages of fatigue life of the composite laminates are obtained based on the evolution of the strain data. The results of SEM analysis on the fracture region due to cyclic loading and failure types are obtained. Finally, the concluding marks of this investigation are reported accordingly. The second section of the study presents, the experimental procedure for preparation of woven fabric laminates is described, and the details of mechanical tests, DIC measurements, and acoustic emission monitoring setup are explained. In the next part, the basics of GAP statistics are given and the analysis approach for acoustic emission data are reported. The results of acoustic emission clustering are presented, and

each acoustic cluster is attributed to specific damage inside the laminates. Also, damage evolution and accumulation is analyzed based on energy release during mechanical tests. In the next section of the paper, results of the DIC technique are presented for tensile tests and compared with SEM images from fractured surfaces of samples. Finally concluding marks regarding observations of the investigation are given.

CHAPTER 2

2. Literature review

2.1. Scope

Piezoelectric materials have a tendency to convert the mechanical signal into an electrical signal and vice versa. Traditional ceramic-based piezoelectric crystals such as Barium Titanate, Lead Zirconate Titanate (PZT) are commonly used as sensors for alarms, motors, vibrations, and sonar waves because of their high acoustic impedance, but they cannot be used as biomedical sensors and are not capable to embed inside the structures[52]. However, many studies found that polymers such as Nylon11, polyvinyl carbonate (PVC) and polyvinylidene fluoride (PVDF) have piezoelectric natures as they are flexible, lightweight and easy to fabricate. A lot of research work is still ongoing for the utilization of these sensors for sensing applications. MIT is working on the development of wearable devices and intelligent clothing by using piezoelectric materials. Some of their researchers are working on the development of PVDF based gastrointestinal devices. As traditional ceramic-based piezoelectric sensors are rigid in nature, these PVDF sensors are flexible and can sense the mechanical deformation associated with gastro activity [53, 54]. Ceramic-based piezoelectric sensors are widely used for Structural Health Monitoring (SHM) of structures. These sensors are used as ultrasonic sensors to actuate and transduce the guided lamb waves and ultrasonic waves to identify the crack inside the structure and components of stiffness matrix which can be used to determine the modulus of material without performing non-destructive testing. Stanford structure and composite laboratory is working on the development of piezoelectric embedded structures such as wings of aircraft for the SHM. They are also working on the development of the smart car by employing piezoelectric material for multifunctional energy storage applications [55]. Recently there was a TEDx talk about the importance of piezoelectric polymers. One of the ideas which presented in the talk was that piezoelectric plates/sheets can be embedded inside the road, so they can provide the information about the damage of the roads. Apart from it, these materials do not need any external system for power generation so the charge that will generate due to the pressure of vehicles can be stored and use as electricity. Cranfield university researchers are working on the development of printed piezoelectric based electrode. These electrodes can be printed on the surface of prepregs as negative and positive electrodes then prepregs can be pressed to produce a smart composite structure. There is a recent trend of

unmanned air vehicles (UAVs) and MAVs in the field of defense and space. In UAVs, missiles, military vehicles and MAVs electric power and the onboard place is a major concern. For example, a microsatellite should operate less than 100W of power consequently allocated power to each actuator is 0.1W to 10W. The actuators used in military and space applications are required to produce high output to mass ratio and should be able to withstand shocks and launching vibrations[56]. Thin PVDF sensors are flexible, easy to fabricate and do not need any external excitation system which make the possibility of their usage for structural health monitoring applications and energy generation by embedding these sensors inside the structures.

2.2. Piezoelectricity

Piezoelectricity is a Greek word used for “pressure” electricity, discovered by Curie brothers. Piezoelectric materials belong to the class of materials which produce an electrical charge when subjected to mechanical loading, similarly, these materials change their dimensions as the consequence of the electrical field. This phenomenon was observed in Quartz crystal which changed its dimensions when subjected to the electrical field. For the first time, Quartz based transducer was used for sonar applications for underwater applications. Now piezoelectric polymeric sensors have a market worth of around 18 billion Dollars.

Piezoelectric materials are from ferroelectrics family. These materials have reversible polarization by strong electric field [57, 58]. Piezoelectric materials are naturally polarized or can be polarized by the exposure of certain conditions. The piezoelectric response of a material mainly depends on the molecular arrangement of the material. These materials exhibit third rank tensor properties which only depicted by acentric materials [59]. These materials are crystalline materials and their molecules have tendency to take collective net measurable against any action. If crystals are not arranging in a specific orientation, then the net response will be zero. Almost all material whether they are conductors or insulators is electrostrictive. The contraction or expansion response can be observed from any material as a consequence of the applied electric field. Piezoelectric materials only change their dimension in one or two directions due to their asymmetric nature. This response is much powerful as compare to electrostrictive materials which make them useful for sensing applications [60].

2.3. Piezoelectric polymers

Piezoelectric polymers have gain importance due to their unique properties which are associated with the arrangements of their molecular chains. Although piezoelectric polymers are not much electroactive as compare to single crystals-based inorganics, they have certain advantages such as chemically resistant, highly efficient and flexible. Polymers can be manufactured at low temperature into complex shapes. Among all polymers exhibiting piezoelectric effect, polyvinylidene fluoride (PVDF) has the best piezoelectric response. PVDF is a fluoropolymer that was synthesized by E.I. du Pont de Nemours and company after the serendipitous discovery of Poly tetrafluoroethylene (PTFE) [61, 62]. Table 1 depicts the comparison among the properties of smart materials.

Table 1. Comparison of the properties of smart materials [63, 64].

Properties	Piezoelectric Polymers	Piezoceramics	SMA
Strain due to filed	2-5%	0.1-0.3%	≈ 8%
Actuation force	0.1-3MPa	30-40MPa	≈ 700MPa
Density	≈ 2.5 g/cm ³	≈ 8 g/cm ³	≈ 6 g/cm ³
Reaction speed	μsec - sec	μsec - sec	Sec - min
Nature	elastic, resilient	brittle	elastic

Piezoelectric polymers have a potential advantage compare to other smart materials as their manufacturing is cost effective and power saving. The piezoelectric coefficient of PVDF is about 20 times higher to conventional ceramic based smart materials. A comparison between the piezoelectric constants of piezoelectric materials is listed in table 2. The negative sign with the piezoelectric constant of PVDF is due to its Poisson's ratio which depicts the relation between the thicknesses of a material due to compression to the expansion in the plane direction.

Table 2. Piezoelectric constants of smart materials [65].

Name	Piezo constant (pC/N)	Piezo strain/volt (Vm/N x 10 ³)
Quartz	2.3	50
BaTiO ₃	191	12.5
PZT	289	25.1
PVDF	-33	-339

2.4. Polyvinylidene Fluoride

Polyvinylidene Fluoride (PVDF) is a semi-crystalline polymer having half crystalline phase while the other half is amorphous. It is synthesized by free radical polymerization of 1,1-difluoroethylene. Water is used as a medium for synthesis along with peroxy compounds which act as a catalyst [65]. The structure of the monomer is shown in figure 1. Besides its piezoelectric properties, PVDF is chemically resistant to organic solvents and has high modulus compare to others. Due to its low dissipation factor, dielectric strength and high permittivity PVDF can be used as a dielectric material.

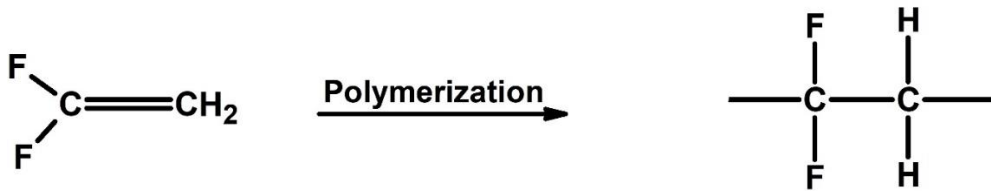


Figure 1 Vinylidene fluoride polymerization

A perfect PVDF molecule has all carbon atoms bonded with fluorine and hydrogen atoms. However, a small fraction of monomers reversed to a polymer during synthesis which is termed as defects. These defects categorized as head to head (CF_2) or tail to tail (CH_2) units and concentration of them depends on the quality of synthesis [66]. At higher concentration of monomer inversion, the β -phase becomes energetically stable which leads to the higher content of β -phase [67]. The β -phase crystalline structure of PVDF is responsible for ferroelectric behavior.

2.4.1. Crystal structure

PVDF has five crystalline phases, these phases categorized on the basis of configuration of $-\text{CF}_2-$ and $-\text{CH}_2-$ in polymeric chains. All of these phases have a certain orientation of atoms which depends on the processing and polymerization process. Figure 2 illustrates the orientation of different phases of PVDF. Some of these phases are electroactive while some are non-active. Each phase has certain applications, but α -phase is the most common phase. The high temperature is desirable for the α -phase above 70° temperature any phase of PVDF can be transformed into α -phase, but it is a non-active phase. The β -phase has ferroelectric nature which only found at a lower temperature.

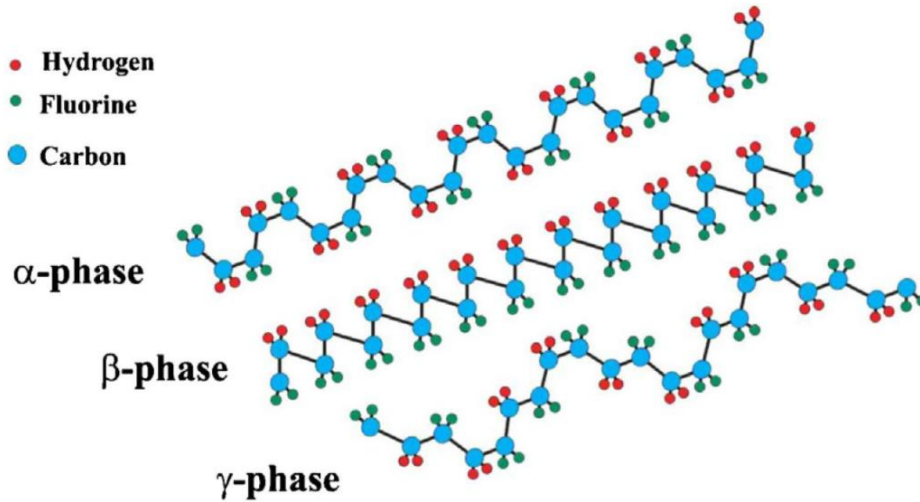


Figure 2. Different phases of PVDF[68]

2.4.2. α -phase

The α -phase is a thermodynamically most stable form which contains alternating Trans-Gauche (TGTG') with monoclinic unit cell ($a=4.96 \text{ \AA}$, $b=9.64 \text{ \AA}$, $c=4.62 \text{ \AA}$ and $\beta=90^\circ$). It crystallizes at all temperatures. It is a nonpolar phase due to the arrangement of atoms and does not depict ferroelectricity.

2.4.3. β -phase

The β -phase is the main phase which has all Trans (TTTT) planar zigzag configuration having an orthorhombic unit cell ($a= 8.58 \text{ \AA}$, $b=4.91 \text{ \AA}$, and $c= 2.56 \text{ \AA}$). It is the most extensively used due to its ferroelectric nature. The fluorine atom is responsible for all Trans conformation because of its size. The c-axis repeats itself in a zigzag manner which is attached to the carbon backbone chain. The β -phase obtained through the drawing of α -phase. Stretching under the influence of high electric field strength renders the piezoelectric properties of the β -phase due to the reorientation of dipoles.

2.4.4. γ -phase

The γ -phase is the third phase which contains (T3G+T3G-) configuration having an orthorhombic unit cell. This is an intermediate phase between α -phase and β -phase. The γ -phase forms due to melt crystallization above $160 \text{ }^\circ\text{C}$.

2.4.5. δ -phase

The δ -phase is the polar phase which is also termed as the polar phase of α -phase formed due to stretching in the presence of the electric field. The dimensions of the unit cell are similar to α -phase the only difference is in the packing of chains.

2.4.6. ϵ -phase

The ϵ -phase also termed as the polar phase of γ -phase. It is a hypothetical polymorphism with has T3G+T3G- an orientation which resembles with γ -phase but in anti-polar arrangement [68].

2.4.7. Stretching of PVDF

The PVDF chain has a coupling of positive and negative charge which is also referred to as dipoles. The fluorine atoms have a negative charge which is bonded with the positive hydrogen atoms. These dipoles are strongly bonded with the backbone of carbon atoms and the orientation of each phase depends on their crystal structure. The β -phase has high polarity and all trans structure aligned the fluorine and hydrogen atoms to produce a unit cell with net polarization [69]. Naturally, β -phase has a zero net charge due to the random orientation of dipoles, however, when it is subjected to strong electric field such as electrospinning process the dipoles of PVDF align themselves in a net positive charge. Figure 3 illustrates the dipole alignment of PVDF β -phase. In oppose to it the α -phase has a disorganized unit cell.

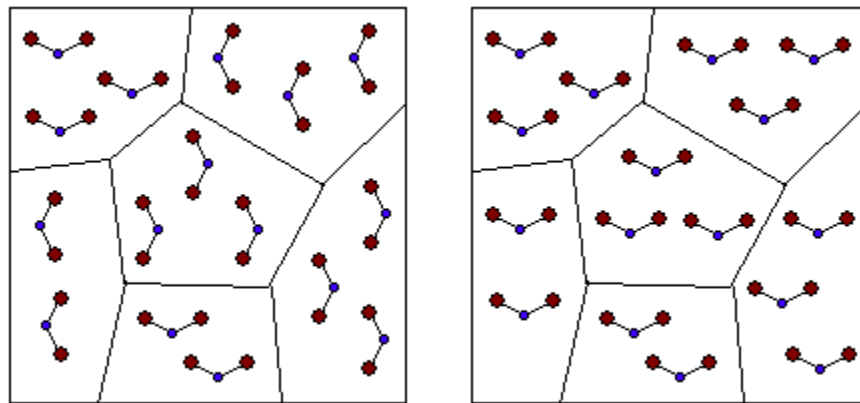


Figure 3 Random and aligned orientation of dipoles of PVDF β -phase[70]

The polarization is directly proportional to the applied electric field. Poling process needs the electric field of 20MV/m and temperature about 100⁰C. The response of polarization can be achieved at any temperature, but the better response obtained at a lower temperature. Polarization

at lower than 70⁰C can yield non-uniform distribution inside the film while the uniform polarization achieved due to the electric field applied to above 90⁰C temperature. The polarization of β -phase is stable up to 140⁰C [70].

2.4.8. Phase transformation

The PVDF granules have spherulites shape grains which are formed by melt constitutes of α -phase with a low fraction of γ -phase. It has semi-crystalline nature due to α -phase which crystallize at the temperature range of 110-156⁰C. However, the β -phase crystallize lower than 80⁰C. The confirmation of different phases is highly dependent on the processing conditions such as temperature, electric field, mechanical and thermal treatments. Figure 4 depicts the relation between the structures of α , β , and γ phases.

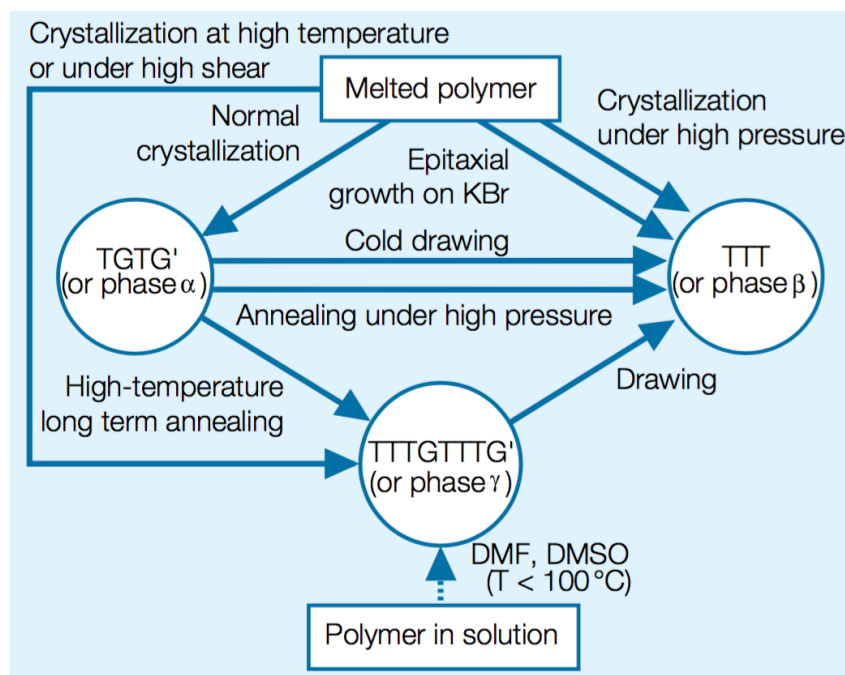


Figure 4. Phase transformation process of PVDF [71].

The α to β phase transition occurs due to mechanical deformation which is also an objective of this dissertation. The transformation decreases with the increase in temperature. The temperature below 80⁰C is favorable for β -phase while the temperature around 130⁰C yields α -phase. The efficiency of phase transformation is 300% between 70-80⁰C [72]. There are various other methods such as polymer additives, copolymers, blends, and ultra-quenching which enhance the transition

of α to β phase [73]. The β -phase formed due to mechanical stretching of PVDF solution under the influence of a high electric field with the help of the electrospinning process[74]. Figure 5 depicts the phase transformation of PVDF due to stretching. In the electrospinning process, the solution ejected from the nozzle under the influence of high electric field which causes stretching of fibers and aligns the fibers. These stretched and aligned fibers are collected at a collector. This is the most efficient method for the phase conversion of PVDF.

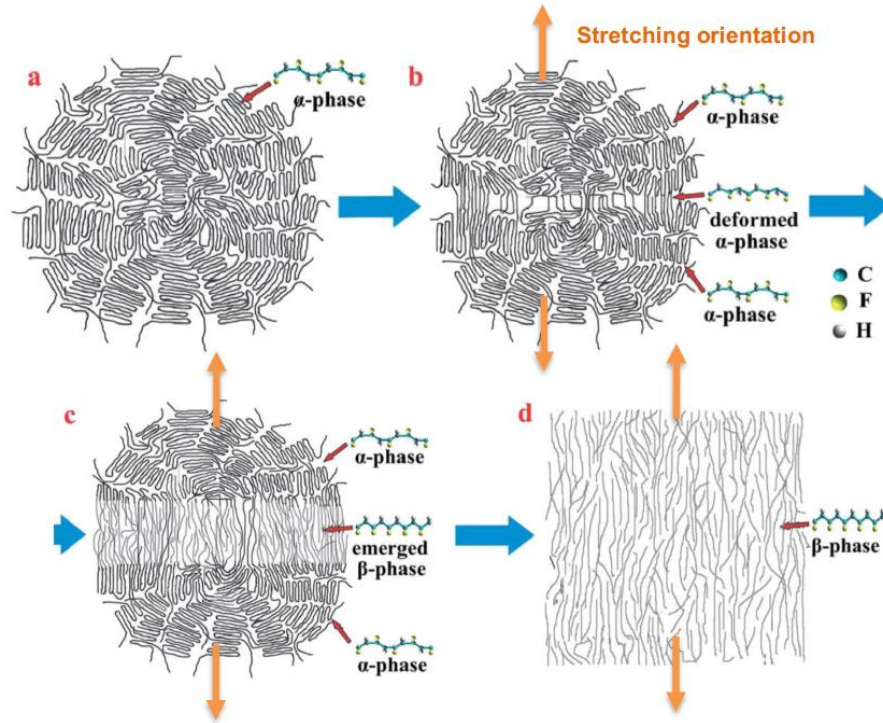


Figure 5. Phase transformation of PVDF due to stretching[75].

The piezoelectric phenomena of PVDF depend on the orientation of dipoles among its crystalline phase. The fluorine atoms are a key player as they attract electronic density towards them as pushing away from carbon atoms which leads to strong dipoles in the C-F bond [75].

2.4.9. Properties

PVDF is a semi-crystalline polymer having tough nature which makes it favorable for engineering applications. PVDF has good chemical resistance even for nuclear radiations, high impact, tensile and dynamic strength. It is thermally stable and abrasion resistant. Table 3 typifies the physical and thermal properties of PVDF

Table 3. Properties of PVDF

Name of property	Values
Water absorption	< 0.04%
Density	1.78 g/cm ³
Melting temperature	175 ⁰ C
Glass transition temperature	-30 ⁰ C
Softening temperature	145 ⁰ C
Crystallization temperature	137 ⁰ C

2.5. Fatigue Testing

Fatigue is termed as a failure of a material under cyclic loading. The progressive structural change permanently occurred inside the material when imperil to fluctuating stress which causes damage accumulation or fracture after a certain number of cycles. Fatigue inside a material occurs due to cyclic load having stress values at a certain stress level. As the number of cycles increases, material undergoes permanent degradation due to fatigue which decreases the stiffness of the material. The value of stress acting on the material is an important parameter to predict the life of a structure. If a stress level is lower, the material will withstand a higher number of cycles but if the stress level is high then it will reduce the materials life. This relation between stress and number of cycles can also be depicted in the form of the S-N curve. Figure 6 shows the effect of different stress level on the lifetime of a structure.

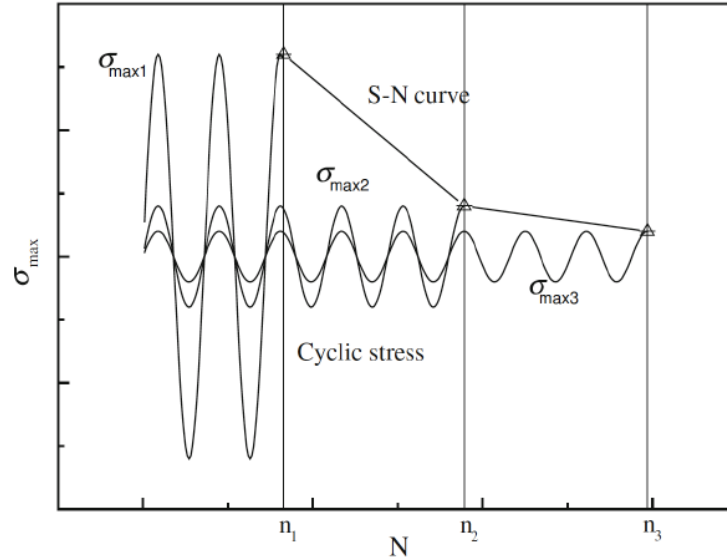


Figure 6. S-N curve depicting the effect of different stress level on the life of a material [76]

Table 4. Important parameters for fatigue testing

Name	Unit	Definition
σ_{\min}	MPa	The lowest stress during fatigue testing is known as minimum stress
σ_{\max}	MPa	The highest stress during fatigue testing is known as maximum stress
σ_a	MPa	The amplitude stress is $\sigma_a = \frac{\sigma_{\max} - \sigma_{\min}}{2}$
σ_m	MPa	The mean stress is $\sigma_m = \frac{\sigma_{\max} + \sigma_{\min}}{2}$
$\Delta\sigma$	MPa	The stress range is $\Delta\sigma = \sigma_{\max} - \sigma_{\min}$
R	-	The stress ratio $R = \frac{\sigma_{\min}}{\sigma_{\max}}$
f	Hz	The number of cycles per unit time $f = \frac{1}{T}$

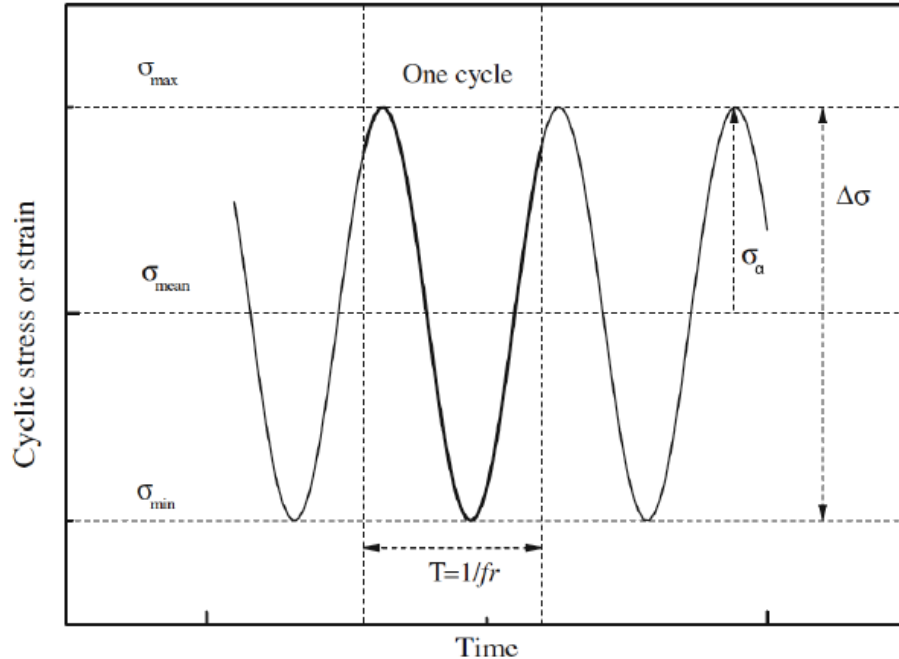


Figure 7 Standard terms for cyclic amplitude loading [76]

Fatigue loading categorized into three types which are based on the maximum and minimum stress.

- Tension-Tension
- Tension-Compression
- Compression-Compression

Tension-Compression loading having positive mean stress is also known as tension dominated testing whereas compression dominated loading has negative mean stress. Figure 8 illustrates the cyclic loading types. Uniaxial constant amplitude loading is not common in structure when it is in service. Instead of uniaxial constant amplitude loading, the multiaxial variable amplitude loading is favorable. Fatigue life prediction models are different for constant amplitude and variable amplitude loading. However, models which are predicting the effect of variable amplitude multiaxial loading is frequently based on the derivatives of uniaxial constant amplitude loading. The fatigue analysis of fiber reinforced polymer composites are presented in the form of the S-N curve[77].

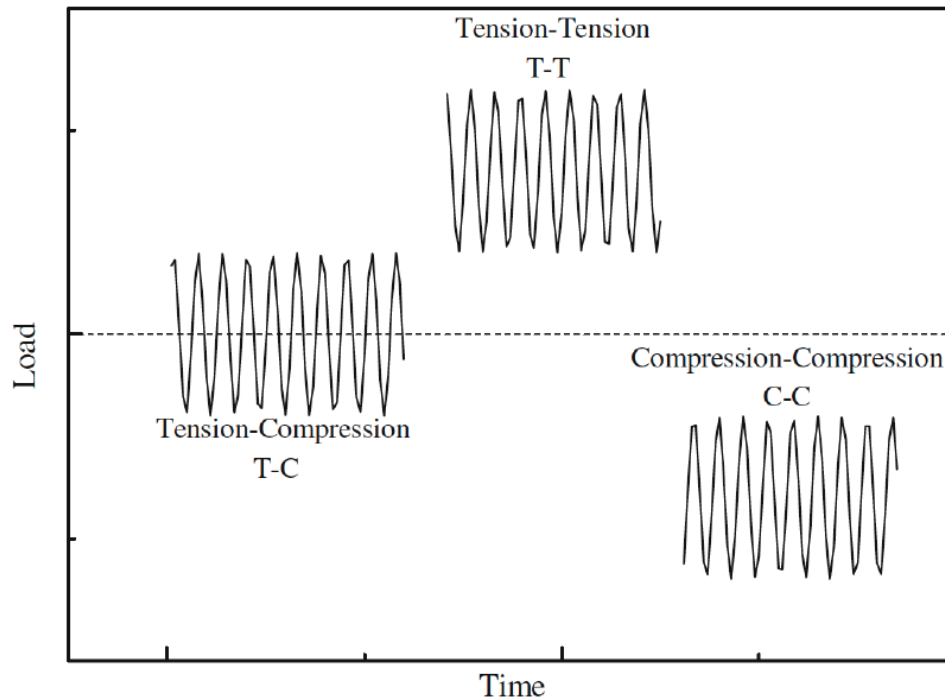


Figure 8. Loading types [77]

2.6. Digital Image Correlation (DIC)

In composite testing, various conventional methods such as extensometer, strain gauges, and different transducers are used for measurement. But these methods only provide the information regarding the selected location of the total gauge length where these are attached or adhered. There are several prominent issues associated with these conventional methods, for example, surface preparation and adherence of strain gauge to the specimen and the strain gauge only provides information regarding the selected area where it adheres. Removal of extensometer before the final failure to protect it from the damage, requirement of surface contact, information from the selected area and sensitivity of sensors and strain gauges. In order to sort out these problems, a non-contact, full-field three-dimensional measurement system was introduced.

DIC is a 3D, full field and non-contact technique which can be used to measure deformation, strain, vibration, and contour on the material. This method can be used for full-field strain measurement for tension, bending and torsion for both dynamic and static measurements, a schematic of the DIC measurement system is exhibited in figure 9. The setup based on high-speed measurement cameras

which have the capability to measure the deformation even at the microscale. It is equipped with stereoscopic sensors which focus each point at a specified pixel in the image plane of the sensor. The position of each point in 3D can be calculated with the help of intrinsic parameters (imaging parameters) and extrinsic parameters (orientation of sensors). By creating a speckle pattern on the surface of the specimen, the position of a point can be identified in the two images with the help of correlation algorithm. DIC techniques gain attention especially in the field of micro and nano scale based mechanical testing due to its ease of use and implementation. Recent advancement in the field of digital cameras and computer sciences have enabled their usage for strain and deformation measurement [78].

Deformation mapping performed by using mapping function which relates the image and can be determined by comparing a set of sub window pair on the whole image. The coordinates (x_i, y_j) and (x_i^*, y_j^*) are correlated by the transformations that happen between the images. If deformation is perpendicular to the camera and very small, then the relationship between (x_i, y_j) and (x_i^*, y_j^*) can be calculated by a 2D transformation.

$$\text{Here } x^* = x + u + \frac{\partial u}{\partial x} \Delta x + \frac{\partial u}{\partial y} \Delta y \quad \text{Equation 1}$$

$$\text{And } y^* = y + v + \frac{\partial v}{\partial x} \Delta x + \frac{\partial v}{\partial y} \Delta y \quad \text{Equation 2}$$

In these equations, u and v represent the translations of the center of a sub-image in X and Y direction. Δx and Δy denote the distance from the point (x, y) to the center of the image. The correlation coefficient r_{ij} is a function of displacement components and gradients of displacement.

$$\text{i.e. } \frac{\partial u}{\partial x}, \frac{\partial u}{\partial y}, \frac{\partial v}{\partial x}, \frac{\partial v}{\partial y}$$

DIC is an effective technique for deformation mapping in mechanical testing, where blotchy pattern provides the contrast for the correlation of images [79].

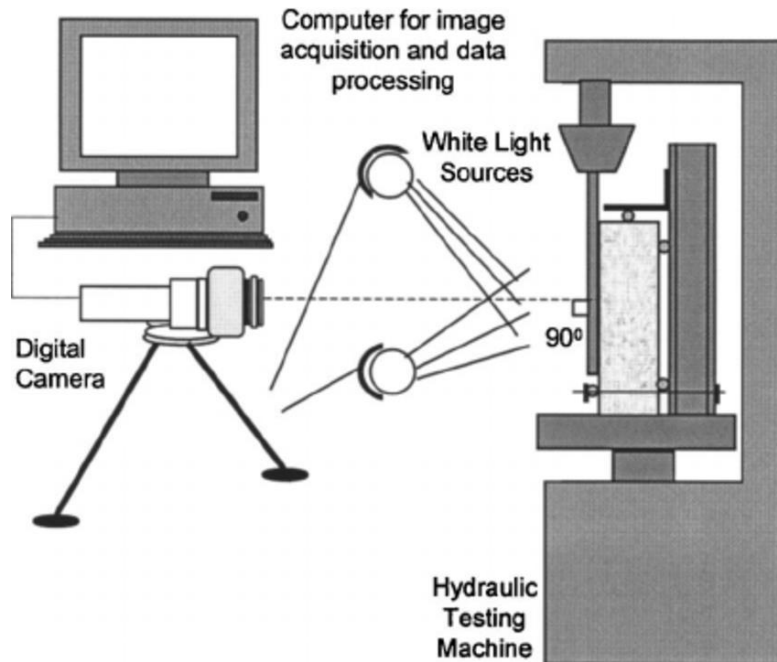


Figure 9. Schematic of DIC measurement system [80]

DIC allows the measurement of displacement of the selected points on the surface of the sample. A speckle pattern is created on the surface of the specimen with the help of paint. DIC sensors were calibrated and these sensors select the blotchy patterns as reference points. These patterns are all over the surface so the DIC select multiple reference points which cover the whole surface. When the load is applied to the specimen, these points displaced from their reference position due to the strain induced inside the specimen against loading. DIC records the displacement against each reference point and provides us the full field strain measurement of the specimen and also the stress distribution trend of the specimen [79, 81]. DIC setup contains two cameras which are calibrated with the help of a calibration procedure which contains 13 steps. Different sized calibration plates are used for the calibration process based on the specimen size. The plate is moved to several positions and angles indicated by the calibration procedure. The calibration procedure provides information to the software to calibrate the volume of the cubical shape which has the face dimension as similar to the size of the calibration plate. The Region Of Interest (ROI) of the specimen should obey the volume of the calibration plate for displacement and strain measurements. After the calibration, the mechanical test is performed by calibrating the DIC with the mechanical testing system, so it will take the snaps at the correlated frequency. The frequency of the system to capture the images relies on the specified data points. There are several parameters

which need to deal with care to get better results. These parameters are facet size, calculation base, facet step, and strain computation matrix size. Increment in facet size figure 10 enhances the precision of point identification without disturbing the sensitivity to the strain deflection but it increases the calculation time.

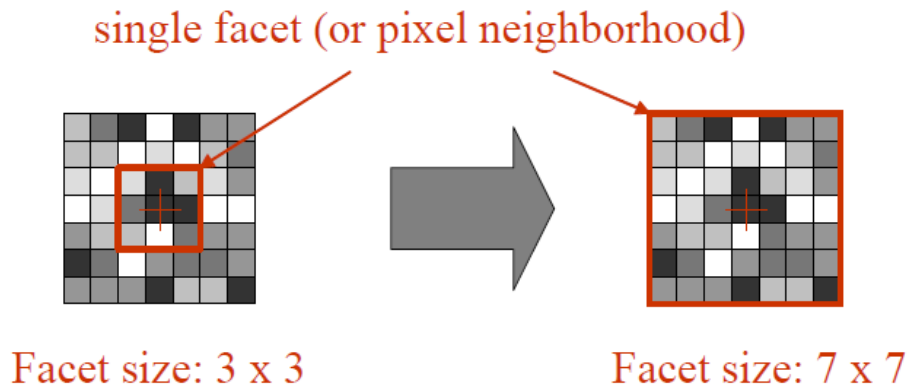


Figure 10. Facet size [82]

The precision of the strain calculation might be increased with the increase of facet step figure 11. This is carried out at the cost of the sensitivity of the strain variation, but it reduces the calculation time. The precision can also be improved by the inflating the calculation base figure 11. The strain of each mesh point is calculated due to relative position change relative to its 8 neighbor points (calculation base value =3). This parameter can be incremented to 5 or higher values according to the practical requirements. This is carried out at the expenditure of sensitivity and calculation time.

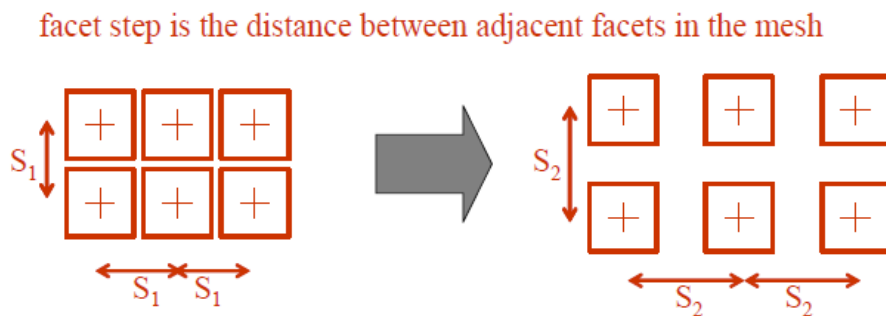


Figure 11 Increment in facet step[82]

Figure – 3 Increase in the Calculation Base

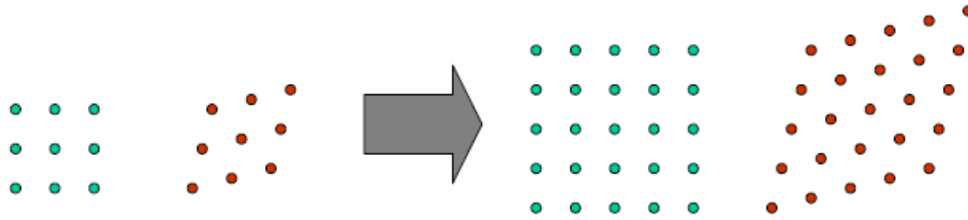


Figure 12. Base calculation[82]

The system identifies the surface of grey scale pattern. Before computing the test, the user can control the computation base, facet step and face size for appropriate measurement. If the area of the specimen is too large, then averaging the strain would decrease the resolution of the test output. In this situation, the concentrations of strain because of the waviness of fibers are just averaged and calculated but not captured. The static analysis of anisotropic materials is used to define the distribution of strain. The strain array contains multiple data points which are distributed all along the ROI. The DIC computes full field all along the surface of ROI. These computed strain values stored in the matrix which is selected for the computational base. This matrix can be rotated and transformed to align it as per fibers direction in the composite sample which provides the better information about the strain as compared to conventional strain gauges which need to be adhered along the angle of fibers orientation [82].

2.7. Acoustic emission (AE)

This testing method used to locate and detect the hidden cracks inside the materials due to the waves generation generated by the redistribution of stress inside the material. This method is similar to ultrasonic testing, but the working principal is different. In ultrasonic testing, the waves are sent through the transducer which we also called as transmitter and then received from the receiver. During the scan, if there is a hindrance in the path of waves it will slow down the wave speed and amplitude will also decrease due to the absorbance of crack. By calculating the difference between non-hindered wave and hindered waves speed we can calculate the crack length. Acoustic emission testing also based on the sound waves, but the sensors usually used during this method are piezoelectric sensors. When a specimen is under stress condition figure 13 then after certain loading value the damage inside the material occurs, which produces sound

impulses of certain energy value which is detected by the sensors. These sound signals are detected by multiple sensors on the surface of the specimen data certain difference of time due to the certain distance between them. The difference of the time provides information about the source of the damage. AE is favorable for a dynamic environment where cracks are produced when specimen experiences the incremental stress otherwise at lower stress value sometimes these activities remain undetected [83]. The AE sensors are mostly piezoelectric sensors which convert mechanical signals to electrical signals which are in the frequency range of 30kHz to 1MHz. Plastic and composite materials have high attenuation so low-frequency signals will be better differentiable.

Acoustic emission analysis provides valuable data about the damage origin and propagation inside the materials which is helpful for structural assessment and its integrity. Acoustic waves are impulses of the pressure which is produced due to the liberation of deformation energy inside the material during the development of a fracture. Acoustic emission setup has a tendency to listen to those vibrations with a frequency range. AE is so sensitive even it can characterize the event which is having very low energy. AE technique considers a nondestructive testing technique as it needs material to be under certain mechanical load value in order to produce damage activities. Keiser effect is the so-called fundamental property of acoustic emission which is named after the person who studied acoustic emission from the materials with the help of electronic setup. These waves are irreversible so cannot be generated during the reloading of the material except the load value does not exceed the previously attained value later another study was conducted which assured that acoustic signals can be generated at the load value below to those previously applied and this is termed as Felicity effect [84]. The waves produced due to stress are traveled from the inner side of the material towards the surface and cause vibration there which are sensed by the transducers. AE signals are classified into three types continuous, burst and mixed. Continuous signals are generated when multiple transients are overlapping each other and cannot be distinguished, and the envelope formed by the amplitude of the signal will be constant. It can be generated by noise or rubbing on the surface of the specimen. Bursts are generated due to damage formation such as delamination and fiber rupture. The mixed signal type usually encountered during the real-time testing which contains both continuous and bursts signals. Acoustic signals which are coming from other sources such as electrical wiring, testing machine are termed as noise. Although noise is a big concern during testing, this noise is located in a frequency range which is lower than the AE

produced due to damage. Piezoelectric transducers especially PZT ceramic based transducers are widely used for acoustic emission analysis due to their broadband range. The vibrations occur due to the damage activities are sensed by the PZT material through a wear plate.

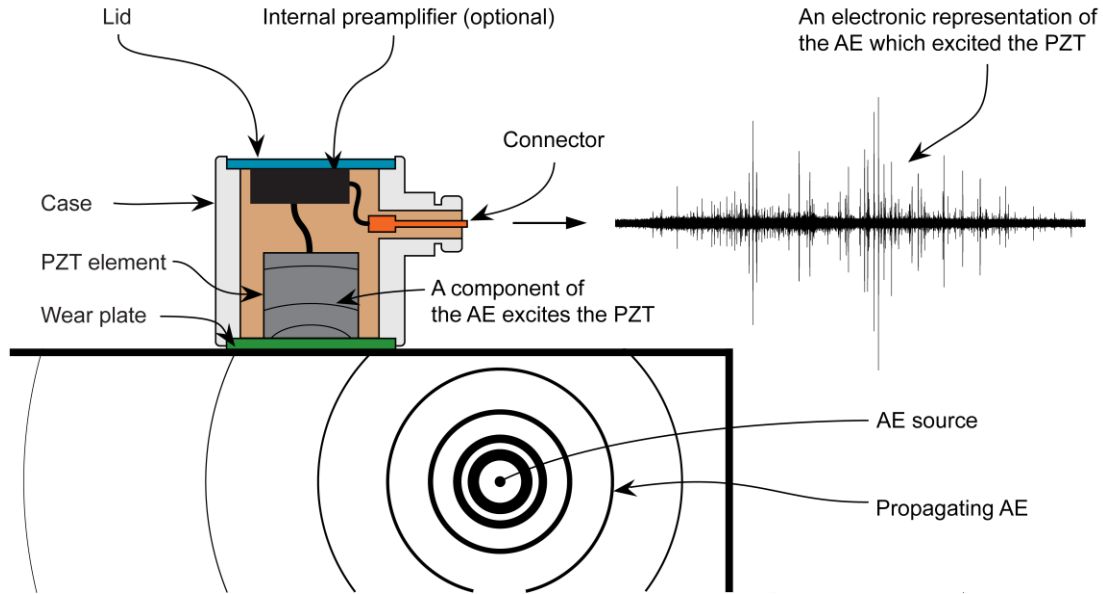


Figure 13. Schematic of acoustic emission testing [85]

Composite specimen's surface, pressure on transducer and medium which is used for coupling are the important factors which impart their effect on the sensitivity of the PZT based transducer [86]. The use of a contact transducer affects the responsive vibrations of the composite. Acoustic emission sensors are designed in such a way that they can detect the activity which is normal to the transducer. The stress components are normal to the direction of the transducer but the responses of the waves coming from different direction will not be identical. The selection criteria for the transducer depends on the response of the frequency curve which is also termed as a calibration curve. AE transducers at lower frequency behave like a displacement sensor but at the higher frequency, it acts as a velocity sensor with the further increment it starts acting as pressure transducer [87]. In the case of the piezoelectric sensor, this transition range is from kHz to a few MHz. In order to calibrate and positioning of the sensor, Hsu-Nielsen source was used. In this method, a pencil lead was broken at the surface of the specimen which acted as a mechanical source. He used Pantel 2H lead having diameter of 0.3mm. Later Inaba and Higo reported that Hsu suggested this procedure with 0.5mm lead the reason behind changing the diameter is that the

properties of lead will also be changed which will provide different AE signals. To produce a consistent acoustic signal a Teflon collar can be put on the tip of the lead pencil [88].

In recent decades, various research projects have been conducted to extract the meaningful information from the signals acquired by acoustic emission analysis. Various researchers extracted data and stored in n-dimensional structures by using several statistical, trending and classification methods which they called as features. These approaches are classified into four types: frequency based, hit based, activity based and waveform.

2.7.1. Activity-based analysis

This is the process for detection of abrupt and trends changes in acoustic emission features with respect to time. The features include in this analysis are signal energy and number of hits [89, 90]. The data usually illustrated by plotting these features as an absolute or cumulative form against time. The ratio of these parameters is also used often when the value of the load is considered as a reference, these ratios are called as Shelby ratio and Felicity ratio. The Felicity ratio was introduced by Dr. Timothy for the indication of damage having mixed results. It is the ratio between the lowest load value which causes the certain acoustic activity to the highest load in the last cycle for dynamic loading[91]. Whereas the Shelby observed the unloading of the composites instead of loading. The Shelby ratio is analogous to the Felicity. Shelby ratio is between the lowest load value that causes certain acoustic activities, during unloading condition, in contradiction to the previous maximum value of the load. This method is useful to classify the acoustic emissions activities produces from friction [92].

2.7.2. Hit-analysis

This analysis uses a certain set of some features or waveforms. Acoustic emission hits are the part of a measured waveform which fulfills the criteria of detection. The aim of this criteria is to ascertain the presence of acoustic hits and discriminate them from the noise or continuous type acoustic signals which are coming from setup or testing equipment. Acoustic hits are transients stress waves so acoustic hits are isolated transient from the waveform which is acquired during the testing. Several techniques are used to determine the AE hits. The most common one in real time parameter based in AE system compares the acoustic signal against the threshold level. Typically, threshold sets on the positive side of the signal, but it can be floating. An acoustic hit is perceived by the comparison of the acoustic signal against the threshold. If the acoustic signal surpasses the level of threshold then that signal will be considered as a hit. This technique has three important

parameters hit definition time (HDT), peak definition time (PDT) and hit lockout time (HLT). The time-based parameter only triggered when a hit crosses the threshold level. If the elapsed time will be equal to the HDT parameter, then hit will be ended. The HLT specifies the time which must be passed after the detection of a hit. The PDT stipulates the allowed time after the detection of time to calculate the peak value. The acoustic hit features contain duration, amplitude, energy, rise time and a number of peaks which cross threshold level [93]. Figure 14 depicts the relationship between these features. The features can be obtained through signal processing such as addition, subtraction, multiplication, and division of multiple features or through filtering, extraction of statistical features such as skewness, kurtosis, and variance. The most widely used hit features-based analysis is trend analysis and often presented as a plot of the cumulative sum of all the features. The trend-based analysis considers as sufficient when the sole purpose is to just monitor the power of acoustic signal which is necessary for some analysis. In most of the cases, the useful information usually extracted by using some statistical features and their comparison with other features.

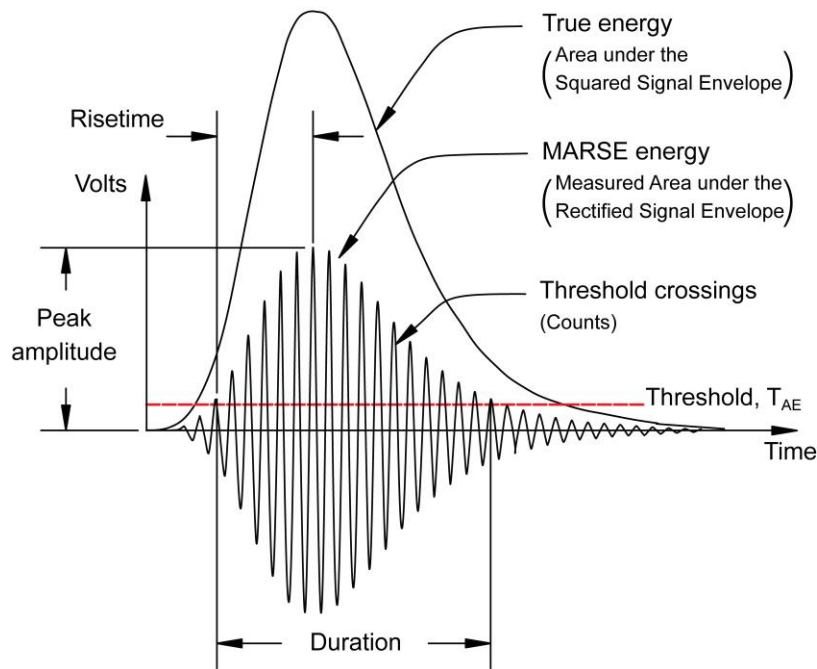


Figure 14. Acoustic emission hit based features [89].

The histogram of the values estimates the statistical distribution of the features. The shape of the histogram provides valuable information, for example, the appearance of the amplitude histogram identifies the damage mechanism. A correlation can be performed by plotting one feature as a

function of other feature for example amplitude vs AE counts, duration vs AE counts and amplitudes vs duration which helps us to identify the mechanism of the damage. The acoustic features reduced data to the useful information instead of the complete waveform which contains a lot of unwanted information. In composite materials, the one damage type can provide a hit with different level of amplitude which makes hard to set the threshold level. Acoustic signals in composite materials experience high attenuation, the signals originate closer to the sensor are stronger as compare to the one away from the position of the transducer. The uneven frequency response of resonating transducer which means that the frequencies of the different features are only spaced about few kHz apart and magnification can have the difference of several decibels [89].

2.7.3. Frequency-based analysis

It involves the frequencies of the acoustic signals for the identification of different sources. Fast Fourier Transform (FFT) is the most common frequency-based analysis which reconstructs the time domain into the frequency domain. Other frequency-based features are peak frequency, power frequency bands and frequency centroid [90]. Acoustic emission signals are time-dependent signals which can also be nonlinear. Power spectrum analysis such as FFT can only depict the distribution of existing frequencies in the signal because FFT is not designed for the analysis of the transient signal. Frequency-time methods are designed to analyze the time-dependent signal. Wavelet Transform (WT) and Short Time Fourier Transform (STFT) are used for discrete signals. The STFT is the window function of FFT which divides the signal into several portions where it is in stationary condition by using a window function which extracts these portions from the signal and then these portions are processed by using FFT. But the limited size of the window causes a problem for the frequency localization. For a defined size of the window, the STFT has a constant resolution for localization for all frequencies and at all times. The localization of the frequency can also be improved by the increment in the window size, but it creates an adverse effect on the time localization due to Heisenberg's uncertainty principle as it refers that we cannot get the accurate localization of frequency and time.

Recently Discrete Wavelet Transform (DWT) analysis for acoustic signal gains much attention as it modified the STFT within the boundaries which are defined by Heisenberg's uncertainty principle. Both DWT and STFT transformation is linear so instead of a fixed window, the DWT refers to a scale window. At higher frequency, the DWT has better time localization but poor

frequency localization and in case of low frequency is it vice versa. The drawbacks of this transformation are it is not time-invariant due to which even a minor shift in the signal can change the coefficient completely and DWT is sensitive to noise as it detects the sharp changes [94].

2.7.4. Waveform-based analysis

It is the study of digitized waveforms shapes and propagation modes. Full waveform and frequency-based signal acquisition requires a lot of space for data storage and offers widespread possibilities of signal processing and data manipulation which provides comprehensive information about failure analysis. Additional information about the material property and damage analysis can be extracted through lamb waves such as modulus of the material. The two modes of lamb waves lowest order symmetric (S_0 or flexural mode) and antisymmetric (A_0 or extension mode) is the propagation modes of these lamb waves which have different properties and their analysis technique is known as modal acoustic emission [95, 96].

2.7.5. Acoustic Emission Analysis

Several researches have been conducted on acoustic emission signal analysis during the testing of composite materials [97–100] These signals categorized damage based on their frequencies such as damage initiation which is arbitrarily located inside the material due to matrix or interface failure which leads towards the second category of signals which specify the damage occurs due to friction activities or delamination which lead towards catastrophic failure which occurs due to the fiber breakage and complete failure of composites. The frequency range between 100 to 350kHz depicts the matrix cracks while fiber breakage was denoted between the 350-700kHz range. The sources of acoustic emission were classified on the basis of a criterion which depicts that 70% of the signal power should be inside the frequency band. If the signal does not fulfill this criterion it means that these signals are due to the debonding. Groot et al. analyzed the frequency spectrum in the range of 50-600kHz and explained that the frequency between 90-180kHz typify matrix cracking, fiber pullout signals are in the range of 180-240 kHz while debonding based signals are in the range of 240 -310 kHz and the frequencies above 300kHz denote fiber breakage [101].

2.8. Scanning Electron Microscopy (SEM)

Electron microscopy is a powerful tool for the morphological characterization of the surface of the failed specimen as it provides valuable information about the reason and modes of failures. As polymeric materials are non-conducting materials which are not favorable for electron microscopic studies unless these materials would be sputter coated with a conducting material. Electron microscope extract information with the help of electron beam which ejects out the electron from the material and provides topographical information about the material. If the material is non-conductive then the electron from the beam will not interact with the specimen and no information will be acquired. Usually, these specimens are sputtered with gold, carbon or platinum through a sputtering process which makes these specimens conductive. SEM provides information about the fractures such as shear imprints, fiber pullouts, fiber breakage, delamination or debonding. This also provides knowledge about the fiber behavior whether it is coated with the matrix or it has a rough surface which can provide information about the fiber and matrix bonding. This information can be compared and used to verify the information obtained from acoustic emission and digital image correlation methods.

CHAPTER 3

3. Dynamic analysis of composites

3.1. Summary

This work presents a comprehensive study about the development of a PVDF based piezoelectric sensor and its characterization by utilizing different techniques. Analysis of the failure mechanism was conducted with the help of a fatigue test and fractography. The correlation factor of the piezoelectric sensor was determined and used for strain measurement then compared with the strain from the extensometer.

3.2. Experimental

3.2.1. Materials

Polyvinylidene fluoride (PVDF) with Molecular weight (Mw) of 180000g/mol, melt viscosity 6000-7500 Poise (100 Sec⁻¹, 230⁰C), and Melt index of 20-35g/10 min (ASTM D1238) was purchased from Sigma Aldrich. Plain weave Toray T300 3K carbon fibers with the areal weight of 200gsm (KCF3KPL200) was procured from Kordsa Company. The mixture of BIRESIN Sika CR 80 epoxy resin and BIRESIN Sika CH 80-6 hardener were used as a matrix where they had the viscosity and density values of (900m.Pa.s, <10 m.Pa.s) and (1.13g/ml, 0.95 g/ml at 25⁰C), respectively.

3.2.2. Development of PVDF nanofibers-based sensor

Polyvinylidene fluoride was dissolved in Dimethylformamide (DMF) solvent at a concentration of 30% wt/vol by stirring the solution at room temperature for 24h, which was followed by heating at 50 ⁰C for 1h and then cooling down to the room temperature (23 ⁰C). The solution was electrospun vertically under the flow rate of 15 μ l/min, the voltage of 18kV and the tip-collector distance of 7cm as shown schematically in figure 15 consequently, forming randomly oriented PVDF fibers ejected from the tip of the needle of the syringe which was collected on the aluminum foil. Folding the aluminum foil enabled us to obtain a capacitor configuration where PVDF fibers acted as dielectric and aluminum worked as electrodes. This capacitor set-up was cut into multiple PVDF sensors with the dimension of 10 mm x10 mm x 1mm and then carefully encased with an adhesive tape.

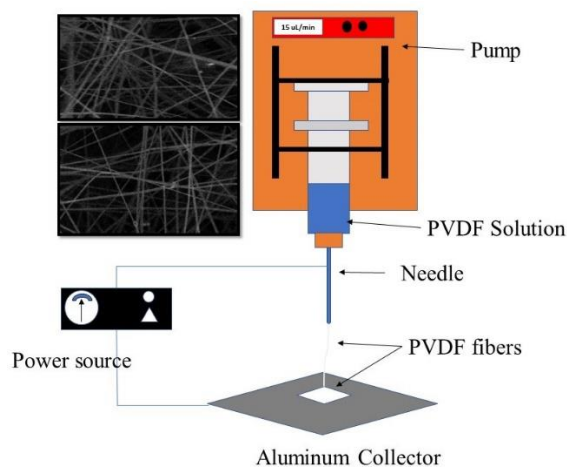


Figure 15. The schematic representation of the electrospinning setup for PVDF nanofibers.

3.2.3. Manufacturing of composite laminate

Sixteen layers of plain weave carbon fibers were used to manufacture the composite plate with the final thickness of 4mm. Dry fibers were cut into the size of 30cm x 30cm using ply cutter (ZÜND G3-L3200). Biresin Sika CR 80 resin was mixed with curing hardener CH80-6 at the room temperature with the ratio of 10:3 wt/wt and degassed for 30 minutes. The cut plies were stacked on a vacuum infusion table, sealed with vacuum bag materials, impregnated with epoxy resin using vacuum injection method, and left to cure for 48h.

3.2.4. Characterization of PVDF granules and fibers

To determine the dipole orientation of PVDF and discriminate among different crystallographic phases, Fourier transform infrared spectrum (FTIR) of electrospun piezoelectric fibers were carried out using a Thermo NICOLET iS50 system. The spectrum of as received PVDF granules and electrospun PVDF fibers was compared to study the change in crystalline structures. Differential Scanning Calorimetry (DSC) as a thermo-analytical technique was used to measure the thermal behaviors of PVDF fibers and granule under a controlled environment. Melting temperature T_m and crystallinity of electrospun PVDF fibers and PVDF granules were determined by DSC through employing METTLER TOLEDO DSC 3+. A sample with a mass of 5mg was placed in Aluminum crucible. The temperature range for DSC was 40⁰C to 250⁰C and the test was performed at the temperature rate of 10⁰C/min under the inert atmosphere of nitrogen purging at 50ml/min. The crystal structure of both PVDF granules and nanofibers was investigated by a D2 Phaser X-Ray diffraction (XRD) system from Bruker. The X-ray beam was Cu Ka ($k = 0.1542$

nm) radiation operated at 20 mA and 40 kV. Relevant data were collected at 2θ ranging from 1° to 30° with a scanning rate of 1° /minute. Morphological changes of PVDF and fracture surfaces of composites were assessed through the GEMINI SUPRA 35vp scanning electron microscopy (SEM). SEM samples were sputtered by Platinum coating. Specimens were attached to the aluminum stub with the help of carbon tape and images were taken at an acceleration voltage of 5KV.

3.2.5. Mechanical testing

The three-point flexural test was performed in accordance with ASTM D790 using 5982 Instron Universal Testing Machine (UTM) on prepared the composite laminate. Three initial samples having the dimension of 15x100x4mm with the span length of 80mm were tested and the following average results were obtained; the flexural strength, failure strain, flexural modulus, and maximum load were respectively, 711 MPa, 1.59%, 50.46 GPa, and 1900N.

Load controlled fatigue test was conducted in a three-point bending configuration on two specimens, namely S1 and S2, having the dimension of 15x100x4mm with the span length of 80mm according to ISO 13003 by using Instron UTM 8803 equipped with 8800MTS Flex test GT controller as schematically depicted in figure 16. A built-in load cell (MTS 661.20F-03) and a video extensometer (MTS. 634.25F-24) were used to collect the load and strain data. A pre-load of 500N was applied to the specimen to remove any form of slack from the load string before the test begins and to ensure that the specimen starts from the same load condition thereby making the data more accurate and much easier to process. The maximum load of 1500N was applied to the specimen with the frequency of 3Hz. For sample S1, one PVDF sensor was embedded between the second and third layer of the specimen from the compression side, while the second sensor was mounted at the bottom surface of the specimen using Poly Ethylene Vinyl Acetate (PEVA) hot melt glue. Sample S2 had only one surface mounted sensor at bottom surface similar to the previous specimen.

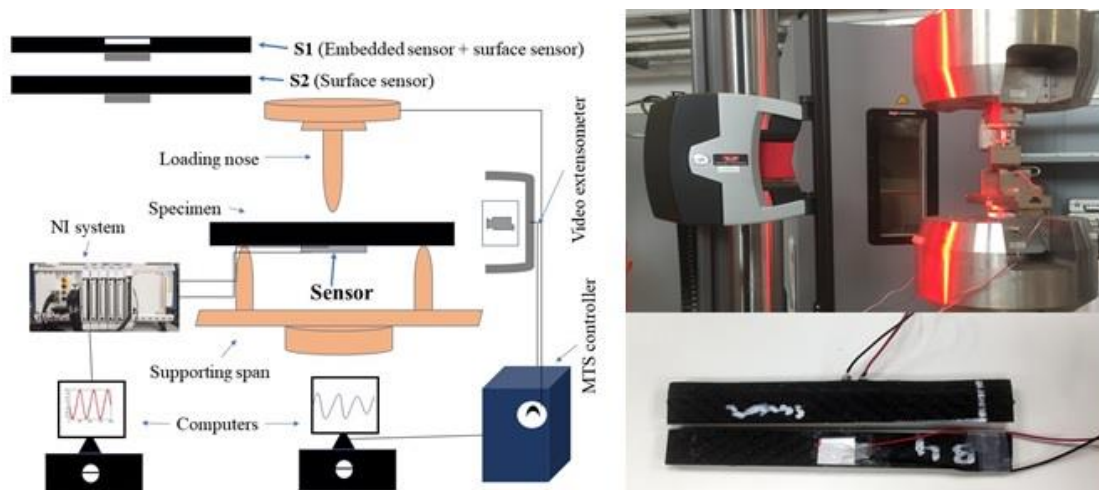


Figure 16. Schematic representation of fatigue testing, testing setup, and specimens.

Piezoelectric response of PVDF sensor due to applied load was interrogated with the help of National Instrument (NI) PXIe-1075 chassis equipped with PXIe-5105 oscilloscope card. NI oscilloscope was triggered by the analog edge signal from the Instron UTM 8803 system to synchronize the data of the UTM and data acquisition systems. The sampling rate of both oscilloscope and the UTM system was 1000 Hz. The response of the PVDF sensor throughout the test was recorded by using NI-signal express and then processed by utilizing NI-DIAdem software.

3.3. Results and Discussions

3.3.1. FTIR analysis

Figure 17 shows FTIR spectra obtained under transmission mode to identify the presence of different crystal structures in the PVDF granule and electrospun nanofibers. The adsorption peaks at 600 cm^{-1} , 765 cm^{-1} , and 796 cm^{-1} are indicators of α -phase crystal which are clearly visible in the spectrum of PVDF granule while absent in nanofiber's spectrum. On the other hand, peak at 840 cm^{-1} is associated with the β -phase crystal in PVDF [10], which is present in both spectra while the spectrum of PVDF nanofibers reveals higher content of β -phase in comparison to PVDF granule. This peak indicates that electrospinning of PVDF promotes β -phase formation due to the stretching of polymeric filament ejected from the tip of the syringe nozzle [102]. The peak at 875 cm^{-1} corresponds to stretching vibrations of C-F bond. The peak around 970 cm^{-1} , being present in the spectrum of PVDF granule but not in that of PVDF nanofibers, indicates the existence of α -phase [103]. The low-intensity peak at 1065 cm^{-1} is related to C=O stretching whereas the peak around 1176 cm^{-1} represents the vibrational motion of CF_2 bond due to centrosymmetric crystal

(TGTG) formation [5]. 1276 cm^{-1} peak is associated with the formation of the γ -phase as both spectra of the nanofibers and the granules have the same amount of γ -phase whereas, 1401 cm^{-1} occurs due to stretching of C-C bond [104].

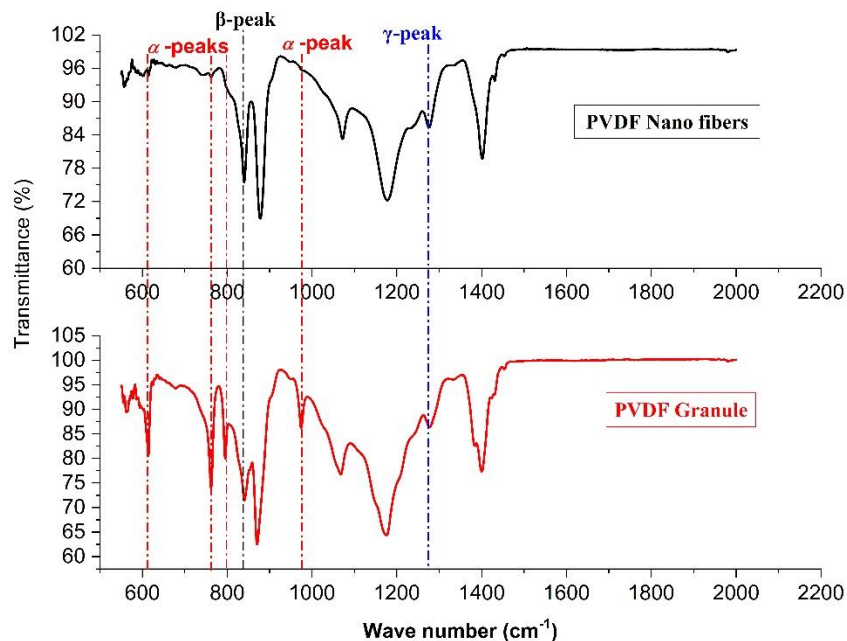


Figure 17. FTIR spectrum of PVDF nanofibers and PVDF granule.

In order to find out the percentage of β -phase content, the absorbance values of α -phase (A_α) and β -phase (A_β) at the wavelengths of 765 cm^{-1} and 840 cm^{-1} for both samples were calculated based on Eq. 3 [10]:

$$F(\beta) = \frac{A_\beta}{(K_\beta/K_\alpha)A_\alpha + A_\beta} \times 100 \quad \text{Equation 3}$$

where K_α and K_β are the absorption coefficient of wavenumbers, 765 and 840 cm^{-1} , having the values 6.1×10^4 and $7.7 \times 10^4\text{ cm}^2\text{ mol}^{-1}$ respectively.

By using the Eq. 1, the β -phase content of PVDF granule and nanofibers were calculated to be 52% and 83%, respectively. It is clearly evident that electrospun PVDF nanofibers have higher β -phase content than as received PVDF granule and the absence of α peaks in the PVDF nanofibers spectrum further confirms the higher content of β -phase in nanofibers.

3.3.2. Differential Scanning Calorimetry (DSC)

In this study, DSC was used to identify the difference in crystallinity among PVDF granule and PVDF fibers. Figure 18 shows heat scans of PVDF granule and nanofibers. Melting enthalpies of PVDF nanofibers (ΔH_1) and PVDF granule (ΔH_2) are measured to be 60.79 joules/gram and 47.9 joules/gram, respectively. ΔH_m is the standard heat capacity of PVDF that is equal to 103 J/g. The percentage of crystallinity can be calculated by using Eq. 4 [105]:

$$C(\%) = (\Delta H_i / \Delta H_m) \times 100 \quad \text{Equation 4}$$

where the subscript i takes a value of 1 and 2.

The melting temperature of PVDF granules and nanofibers are 172 °C and 171°C, respectively. The degree of crystalline for PVDF granules and nanofibers are 46.5% and 59%, correspondingly. The fact that the crystallinity of PVDF nanofibers is higher than that of the PVDF granules is related to the alignment of polymeric chains in the direction of electrospinning due to the stretching of electrospun fibers. The electrospinning process provides sufficient time for the fibers to be stretch and dry properly, whereby fibers are arranged themselves in favorable orientation, hence, converting α -phase into β -phase by changing dipoles of α -phase.

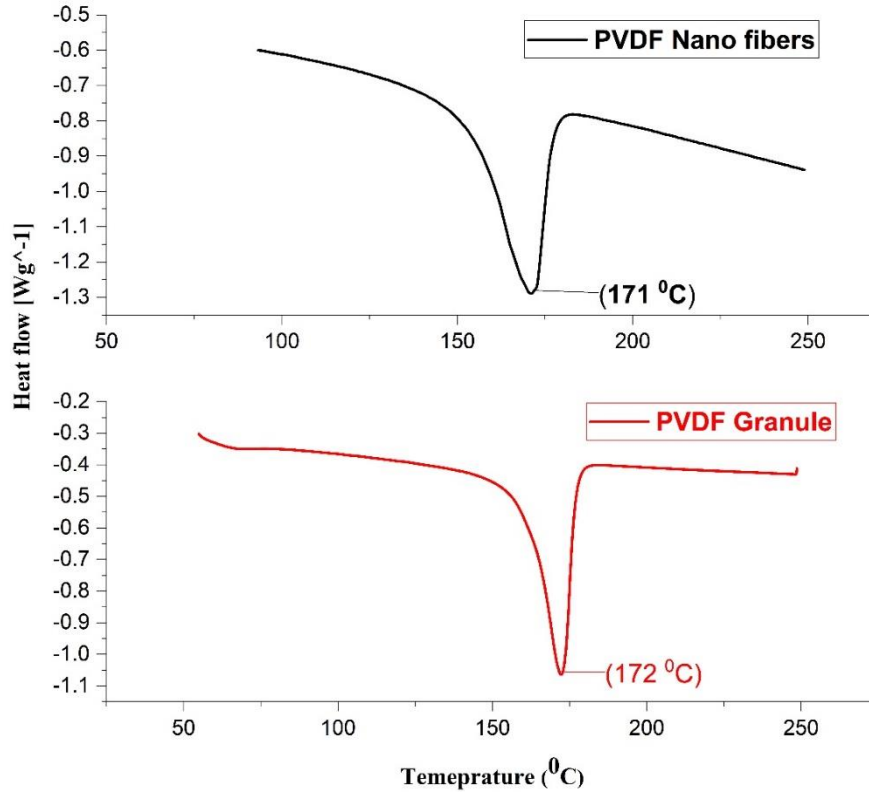


Figure 18. DSC curves of PVDF granule and nanofibers.

3.3.3. XRD Analysis

Figure 19 presents the spectrum of XRD analysis carried out to identify the phases present in PVDF granules and nanofibers. Regardless of the distinctive crystal structures presenting peaks which are similar to each other, some of them are uniquely distinguishable for each particular phase. However, the identification of γ -phase was difficult among all other phases. α and γ phases are easily differentiable from the β phase. β -phase has an intense peak at 20.2° but α and γ phases have peaks around 18° . β -phase that is distinguishable from a well-defined intense peak at $2\Theta = 20.2^\circ$, that is considered to the sum of (2 0 0) and (1 0 0) diffraction planes. α -phase presents characteristic peak at $2\Theta = 18.3^\circ$ which corresponds to the (0 2 0) and (1 1 0) planes [6][106].

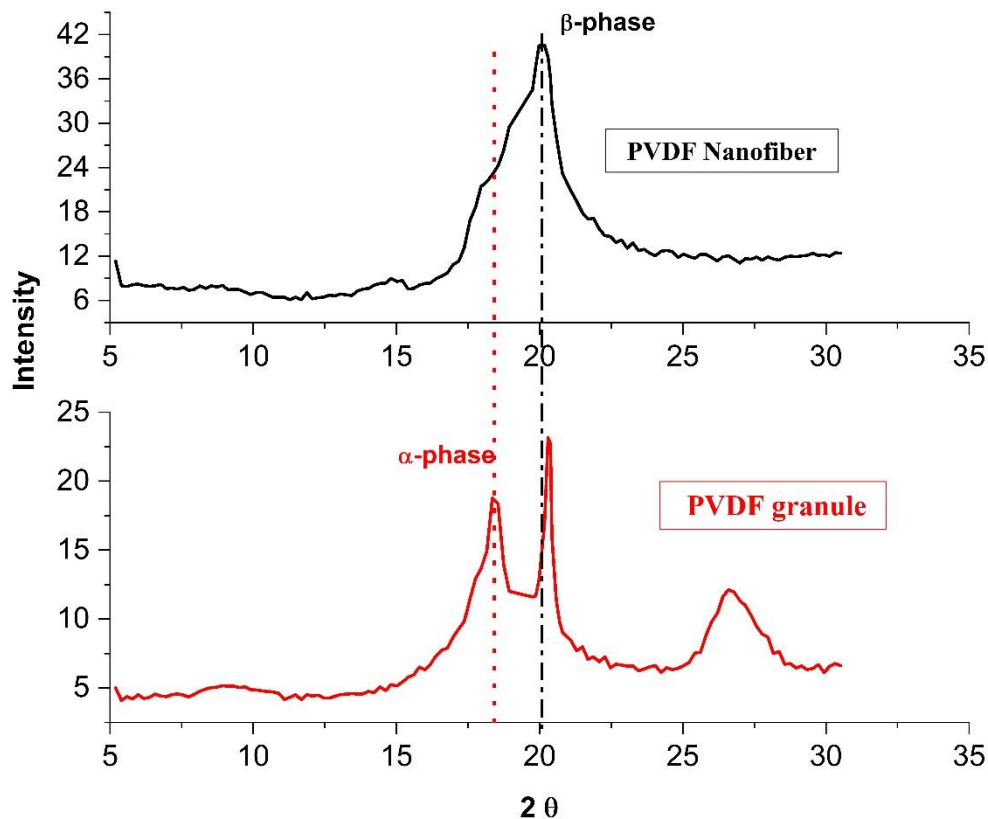


Figure 19. XRD spectrum of PVDF nanofibers and PVDF granule.

The spectrum of PVDF nanofibers exhibits only a single peak around 20.2° , which corresponds to the presence of β -phase. In the spectrum of PVDF granule, there are two visible peaks, namely, the peak at 18.3° belonging to α -phase while the second peak at 20.2° corresponding to β -phase. This observation is consistent with the results of DSC analysis, i.e. dipoles of the polymeric chains are aligned due to the high voltage of the electrospinning process. Hence, XRD analysis reveals the dominant presence of β -phase in electrospun PVDF nanofibers.

3.3.4. Scanning Electron micrographs of PVDF fibers

Figure 20 presents the microscopic images of defect-free randomly oriented electrospun PVDF fibers from two different locations to ensure homogeneity of the fibers. No signs of pores and beads formation are visible in the electrospun nanofiber surface. The high acceleration voltage of 18kV and the flow rate of $15\mu\text{L}$ produce stretched fibers within the diameter range of 30 to 90 nm. 30% wt/vol solution concentration has an appropriate viscosity for the electrospinning process to produce smooth fibers.

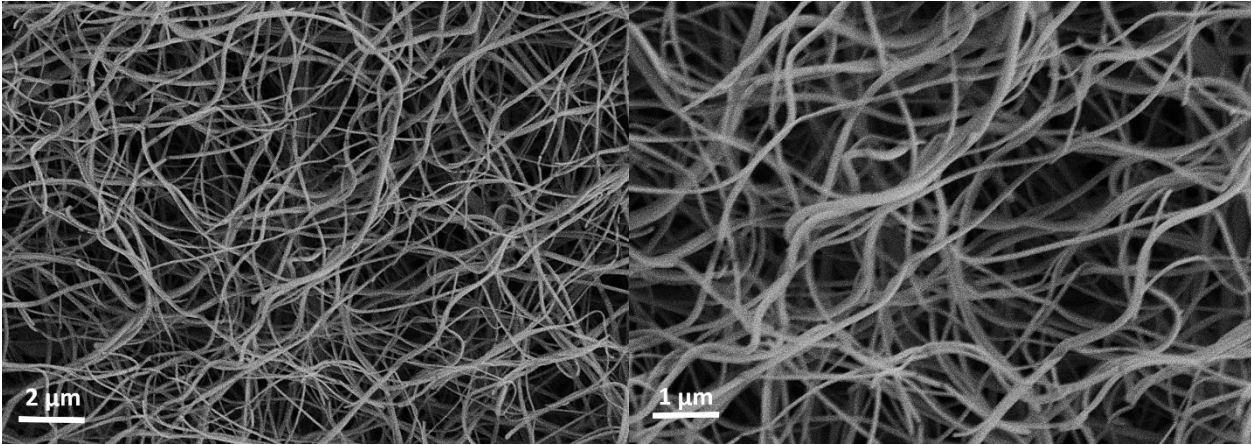


Figure 20. SEM images of PVDF nanofibers.

3.3.5. Fatigue loading and piezoelectric measurement system

Load controlled fatigue tests were performed on two different specimens in three-point bending configuration. The first sample (S1) had two PVDF sensors. One of them is attached to the bottom surface of the composite specimen while the second one is embedded between the second and the third layer from the top surface. The second sample (S2) has only one sensor cohered at the bottom surface. Due to their relatively poor thermal conductivity, composite materials experience autogenous heat generation when subjected to fatigue loading, which can lead to non-uniform temperature distribution and excessive temperature increase within the composite materials. The high temperature may alter the mechanical performance of the composite materials thereby altering their fatigue behavior. In literature, loading frequency ranging from 1 to 5Hz was reported not to have any noticeable detrimental effect on fatigue behavior [107]. Therefore, in this study, fatigue tests are performed under 3Hz frequency. Moreover, the use of low frequency is favorable given that the PVDF sensor needs adequate time for the reorientation of the piezoelectric structure [108].

Figure 21 presents the variation of strain difference between peak and trough values measured by video extensometer for S1 and S2 samples in which one can notice that the S1 experiences a decrease in the strain from the beginning of the test to 15000 cycles, which is unexpected under normal circumstances since for the fatigue tests performed in a load-controlled manner the strain

difference is expected to increase due to the stiffness degradation in the composite material. The drop in the strain until 15000 cycles can be certainly attributed to the damage initiation and consecutive delamination due to the presence of embedded sensor as seen from an SEM image in Figure 21. The specimen S2 shows a gradual increase in strain up to 46960 fatigue cycles due to the reduction in stiffness, which is associated with damage formation. Between 46960 to 51057 cycles, the strain shows a peculiar trend that might be related to a major failure such as delamination between the surface plies and layers underneath. Due to the failure of upper layers, the load is not fully transferred onto the middle and bottom layers hence a notable decrease in strain for a certain number of cycles is observed. As the damage starts to accumulate in the middle and bottom layers, the strain value increases gradually once again from 51057 cycles onwards. The global failure of laminate is inevitable after an excessive buildup of damages in the entire laminate, thereby leading to a sharp vertical rise in the strain value at the last cycle.

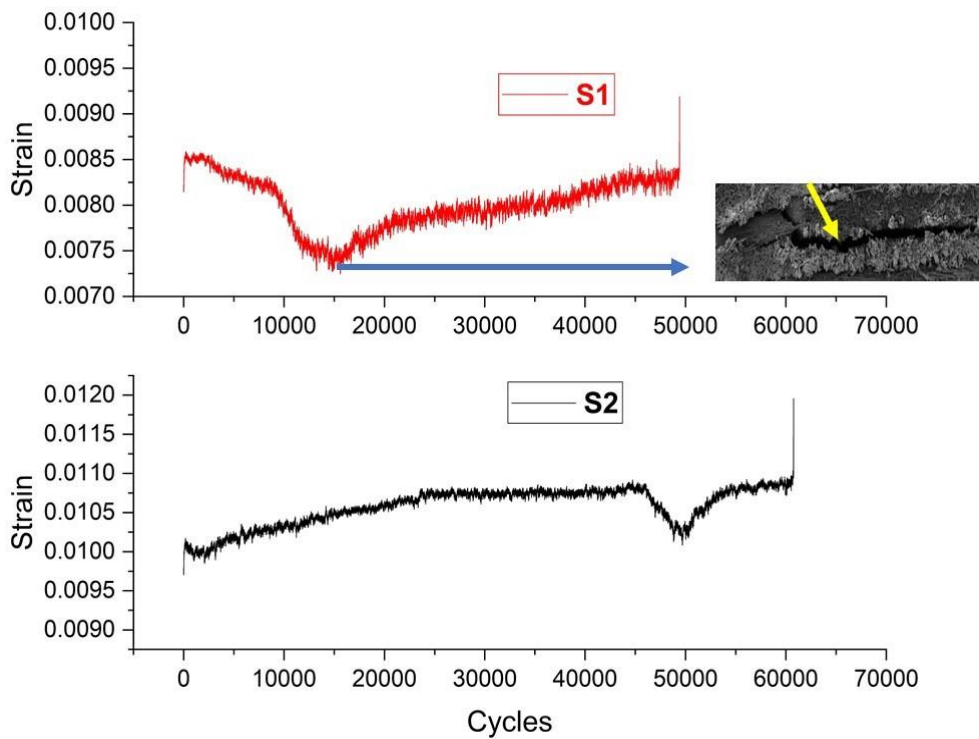


Figure 21. The variation of strain difference between peak and trough values as a function of the fatigue cycle for S1 and S2 specimens.

Surface mounted and embedded PVDF sensors of S1 specimen are compared in terms of their cycle by cycle voltage output, moreover, their capability and performances are correlated with the

strain fields obtained from the extensometer as given in figure 22. It is obvious that the surface mounted PVDF sensor provides smoother and well-tended strain data while the embedded sensor has a quite noisy voltage output. As the embedded sensor is close to the loading head/indenter, it is subjected to higher deformation and in turn experiences degradation in its performance and accuracy. On the other hand, the surface adhered PVDF sensor of the S1 specimen shows a well-behaving response against the fatigue loading because it is far from the loading head. Thus, the deflection of the specimen caused by the loading prompts the deflection in the sensor, which generates the voltage in a response to the change in dimensions due to its piezoelectric nature. In summary, the surface attached piezoelectric sensor has a better capability for damage detection in comparison to the embedded sensor in composite materials.

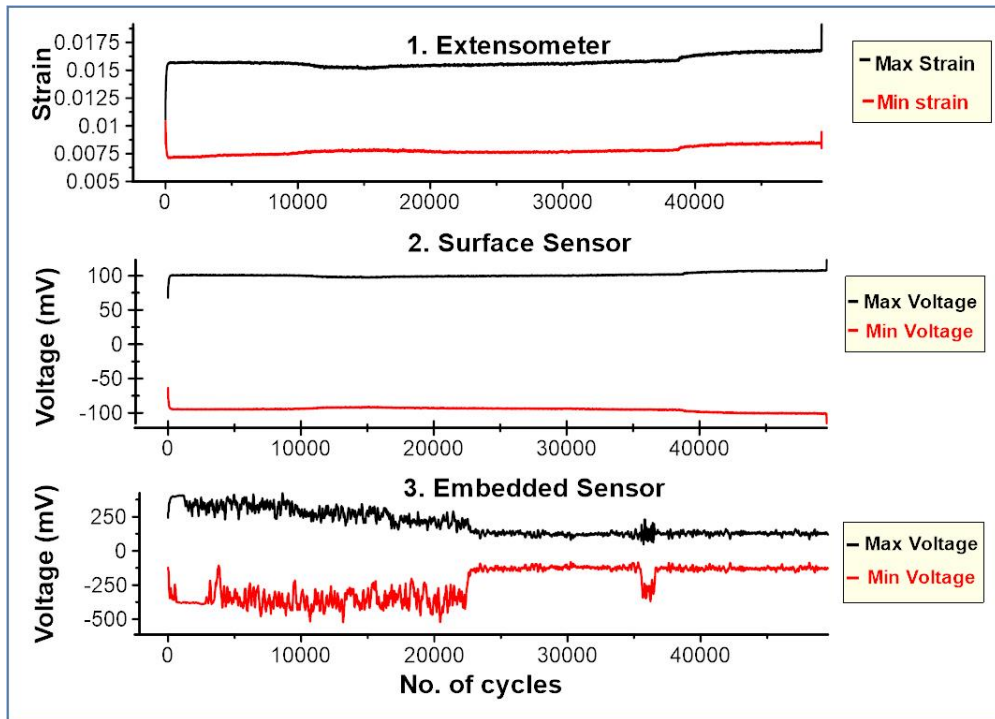


Figure 22. Measured voltage and strain against the number of cycles for S1.

Figure 23a shows the variation of strain measured by the extensometer with time for the duration of one second while Figure 23b indicates the Fast Fourier Transformation (FFT) of strain data performed through NI-DIAdem. The FFT spectrum of the strain versus time data clearly shows the accuracy and reliability of strain measurements through extensometer since there is no spectral leakage, i.e. multiple peaks at frequencies other than 3Hz, which is the fatigue load frequency. Fig. 23c indicates that the difference between the peak and trough values of strain continues to increase

up to 46960th cycle. No abnormalities are observed in this range which assures consistent loading frequency on the sample. The region corresponding to the range of 46960 to 51057 cycles reveal a reduction in maximum strain and an increase in minimum strain, thus confirming a temporary increase in the pseudo stiffness of the sample. As mentioned earlier, the short increase of pseudo stiffness is attributed to damage formation in the surface plies, hence, in turn, causing middle layers to bear the external load. Further increase in the difference of peak and trough strain values corresponds to the gradual accumulation of damages at middle layers and eventually global failure of the material.

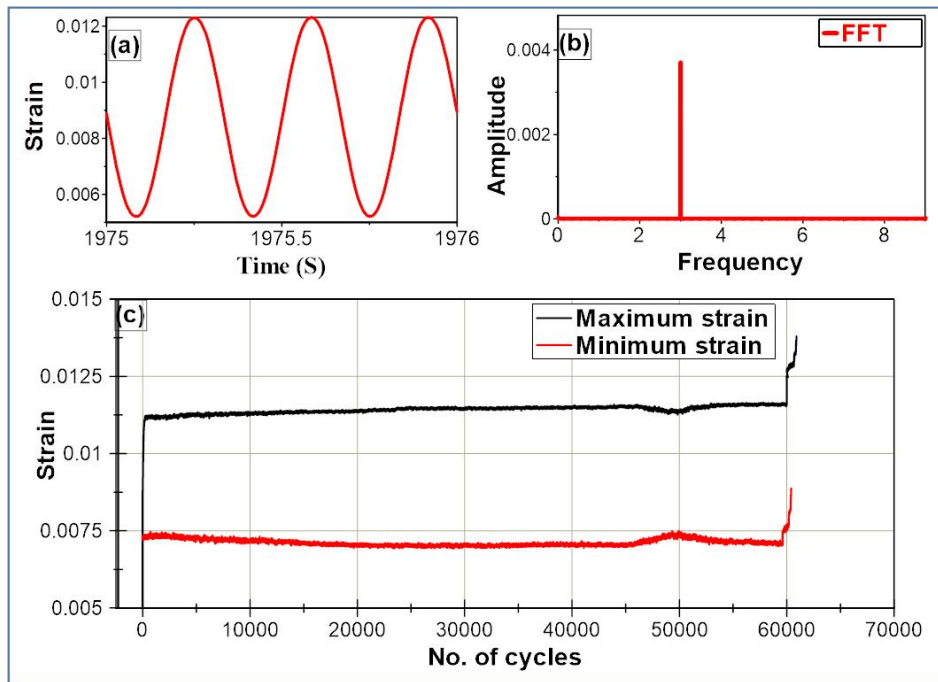


Figure 23. Fatigue evaluation of sample S2: (a) Strain vs time. (b) FFT spectrum of strain vs No. of cycles. (c) Strain vs No. of cycles.

Figure 24a presents the variation of voltage and strain measured by PVDF sensor and video extensometer on S2 specimen for a sampling interval of one second. It is clearly seen that the variation of the voltage in the time domain is identical to the strain variation presented in Figure 24a without any phase difference. The FFT of voltage data given in Figure 24b has a main peak at the frequency of 3Hz, which corresponds to the frequency of the fatigue test, thus confirming the reliability and consistency of data obtained through the PVDF sensor under fatigue loading. It is known that nearly all signals contain energy at both fundamental and harmonic frequencies. If all

the energy in a signal is not contained at the fundamental frequency, then that signal is not a perfect sine wave, as can be seen from Figure 10a. One can see that there is a harmonic peak at 6Hz which is attributed to the backlash of PVDF sensor associated with the reorientation of piezoelectric structure in the sensor during the unloading period since PVDF film tries to maintain its original crystalline phase upon the release of mechanical loading. Since the waveform in Figure 24a resembles sine wave to a larger extent, the amount of energy at harmonic frequency should be rather negligible, leading to small amplitude of harmonic at 6Hz in the frequency domain as compared to the main peak at 3Hz. This affirms that PVDF film-based piezoelectric sensor has the potential to be utilized for strain measurement in structures under dynamic loading. To analyze the electrical response of piezoelectric sensors during each cycle, one can consider the voltage variation during each mechanical cycle. When preload, i.e. 500N, is applied to the sample, the initial value of approximately 21mV is produced in the piezoelectric sensor. Upon the initiation of the test, the load level starts alternating between 500N and 1500N with 3Hz frequency. The amount of voltage and strain obtained respectively from piezoelectric sensor and extensometer denotes a gradual stabilization for the first 200cycles. This instability of values in obtained signals is related to the disability of the UTM machine to synchronize with the target frequency of 3Hz. Thus, the proper values of voltage for maximum and minimum load levels during each cycle are not achieved immediately after the start of the fatigue test. As seen in Figure 24c, peak to trough value of voltage after the stabilization of system is 214mV in which the negative and positive signs of the voltage corresponds respectively to tension and bending of the specimen as a result of cyclic loading [109]. As the test proceeds, the absolute difference between peak and trough values of voltage reaches up to 223mV at 46960 cycles which indicates a considerable decrease in stiffness of composite material due to gradual damage accumulation. The sudden drop and increase in maximum voltage match vice versa behavior in minimum voltage of the PVDF sensor between 46960 and 51057 cycles. As stated previously, the drop in the maximum strain or equivalently in voltage, referred to an increase in pseudo stiffness, due to failure of surface layers and in turn load bearing by the less damaged middle plies. Consequently, the damage accumulation in middle layers promotes another stage of stiffness decrease until the global failure of laminate. This stage is clearly observed with a consistent increase in the voltage difference between the peak and trough values of voltage up to 226mv. Hence, it is seen that voltage variations obtained through piezoelectric sensors agree with strain alteration obtained with video extensometer shown in Figure 23c. The other noteworthy

fact is that the PVDF sensor has a stable response and there is no disruption in the performance of the sensor even after more than 60,000 fatigue cycles. This fact is due to the high flexibility of PVDF sensors which give precise response even at very high cycle fatigue tests [19].

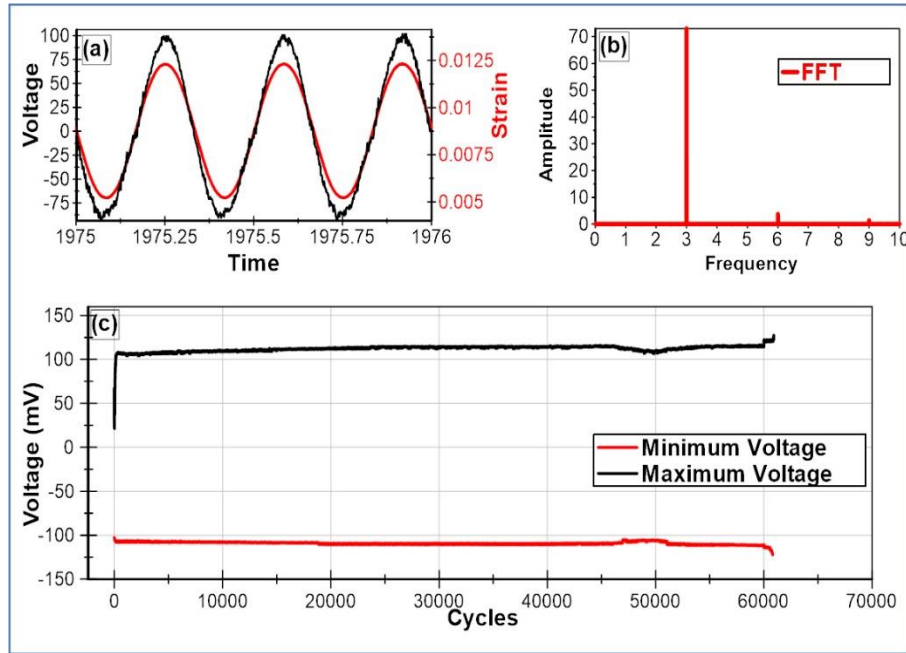


Figure 24. Piezoelectric response of PVDF sensor: (a) Voltage vs time. (b) FFT of voltage vs No. of cycles. (c) Voltage vs Cycles.

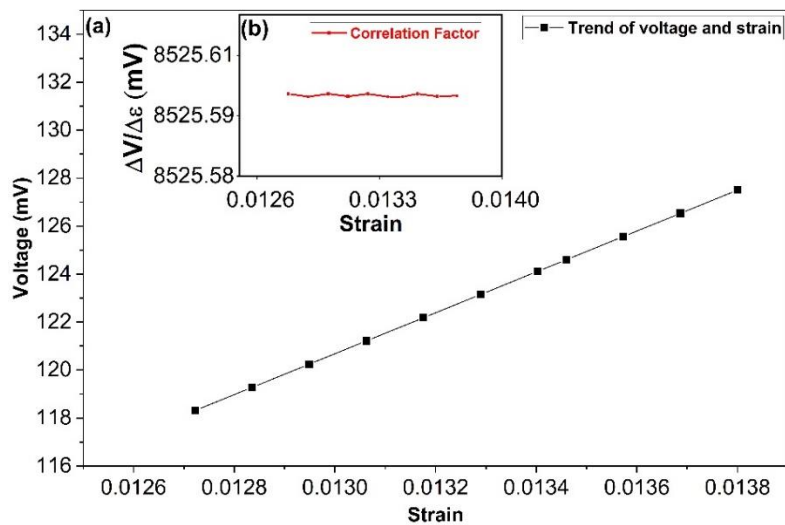


Figure 25. (a) Trend of voltage vs strain, (b) Slope of voltage vs strain plot.

Figure 25a shows the relation between voltage and strain values obtained throughout the fatigue test of sample S2. It is seen that there exists a linear relationship between these two data sets, confirming the ability of PVDF piezoelectric sensor to measure the strain of composite materials during cyclic loading. The inset plot in figure 25b clearly indicates that the slope of the line (i.e. correlation factor) is almost constant with an average value of 8525.55 mV/strain. This factor is used to convert the voltage of in-house PVDF sensor into the strain.

3.3.6. Fatigue Life Prediction using PVDF Sensor

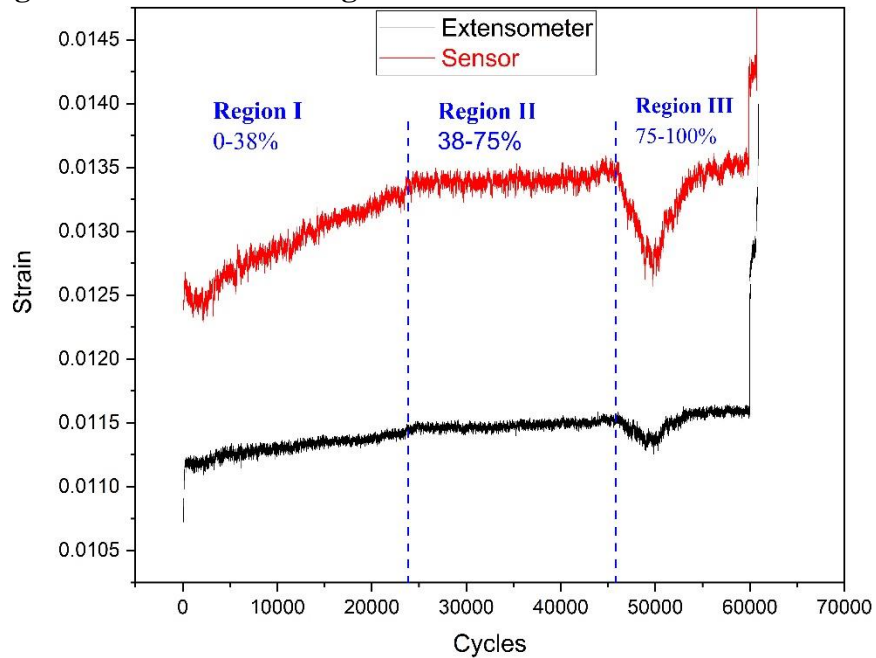


Figure 26. The variation of maximum strain recorded by extensometer and PVDF sensor as a function of the fatigue cycle.

The fatigue life of composites follows a trend with three distinctive regions, which has also been reported by various researchers through other analysis techniques[35, 36]. The first region (Region I) is associated with the matrix dominated damage initiation. At this region corresponding to lower fatigue cycles given in Figure 26. there is a relatively sharp and nonlinear increase in the strain due to damage initiation in the form of matrix cracking and matrix-fiber interface failure, which can be named as intralaminar cracks. In composite materials, about 50% of damage occurs in the first 20-25% of the fatigue life, which implies that a structure can survive with the presence of matrix dominated damage [111]. The major crack occurs as the strain in the specimen goes beyond the failure strain of the matrix. Intralaminar damages are particularly prominent in the specimen

where the orientation of fibers is not along the loading axis as in the case of this study. The second region (Region II) is characterized by a gradual and linear increase in the strain. This can be attributed to stress concentration at the tip of intralaminar cracks thereby promoting their propagation across the adjacent plies of the laminate, and hence leading to interlaminar damage such as delamination. Jollivet et al.[112] stated that the presence of laminae with various fiber directions can cause delamination. Similarly, in the case of woven fabric laminated composites, a small deviation in the direction of weft or warp fibers can cause stiffness change at various points of the same ply, which induces intralaminar failure and thus promote delamination. The final region (Region III) shows a drastic variation in the strain resembling a “valley” before the failure of the specimen. As can be seen from the figure 26 that in Region III, the strain initially drops and then increases. The drop in the strain can be reasoned out with the failure of surface layers which transfers the loads towards the plies underneath accompanied by interlaminar delamination. The strain starts increasing as the applied load is carried by the relatively more intact layers in the middle plies. The further increase in the strain takes place dominantly due to the accumulation of damages. The damage mechanism occurring in this region is also known as a translaminar failure.

The strain calculated by dividing the output voltage of the PVDF sensor by correlation factor shows a similar trend to the one recorded by the video extensometer. All three stages of the fatigue life are well captured by the PVDF sensor. It is important to note that the so-called “valley” region is better resolved by the PVDF sensor. The detachment of strain sensors such as surface mounted strain gages is a big concern during fatigue testing especially when the specimen is subjected to multitude cycles. Due to its flexible nature, the PVDF sensor does not experience any detachment from the surface of the specimen throughout the test, lending itself to effective monitoring of strain field of composite materials under the fatigue loading. Overall, there is about 5 % difference between the maximum value of strain recorded by extensometer and the PVDF sensor, which can be related to the backlash typically observed in the polymer-based piezoelectric sensor.

3.3.7. SEM analysis of fatigue fractured specimen

Due to lower fatigue life of the S1 sample with embedded PVDF sensor, SEM images are taken from two viewpoints of the sample after failure. Figure 27a gives the micrograph taken from the side view of the fracture surface (parallel to the fracture plane) far from the position of the sensor where a large interlaminar crack in between the second and third plies of the S1 sample is visible. This crack is initiated due to the presence of embedded sensor and has propagated all through the

span length of the sample. Eventually, the development of this crack has facilitated the growth of macro damage through the thickness of the sample and early failure of the laminate compared to S2 laminate. Thus, it can be concluded that the embedded sensor has functioned as a defect inside the material, which can aid the creation of interlaminar cracks under cyclic loads. The image in figure 27b taken directly from the fracture surface near the embedded sensor indicates the presence of the same interlaminar crack through the thickness of the laminate. It is worth noting that the size of this interlaminar delamination is bigger than other damage types such as the fiber rupture and delamination just adjacent to it. According to a study by Isherbini et al.[113] the presence of gaps (i.e. cracks) inside the fiber reinforced laminates can result in high interlaminar stress at tips of the crack and growth of gap. The embedded sensor acted as a defect similar to a gap inside the laminate whereby an interlaminar crack due to the presence of high out of plane stresses is developed.

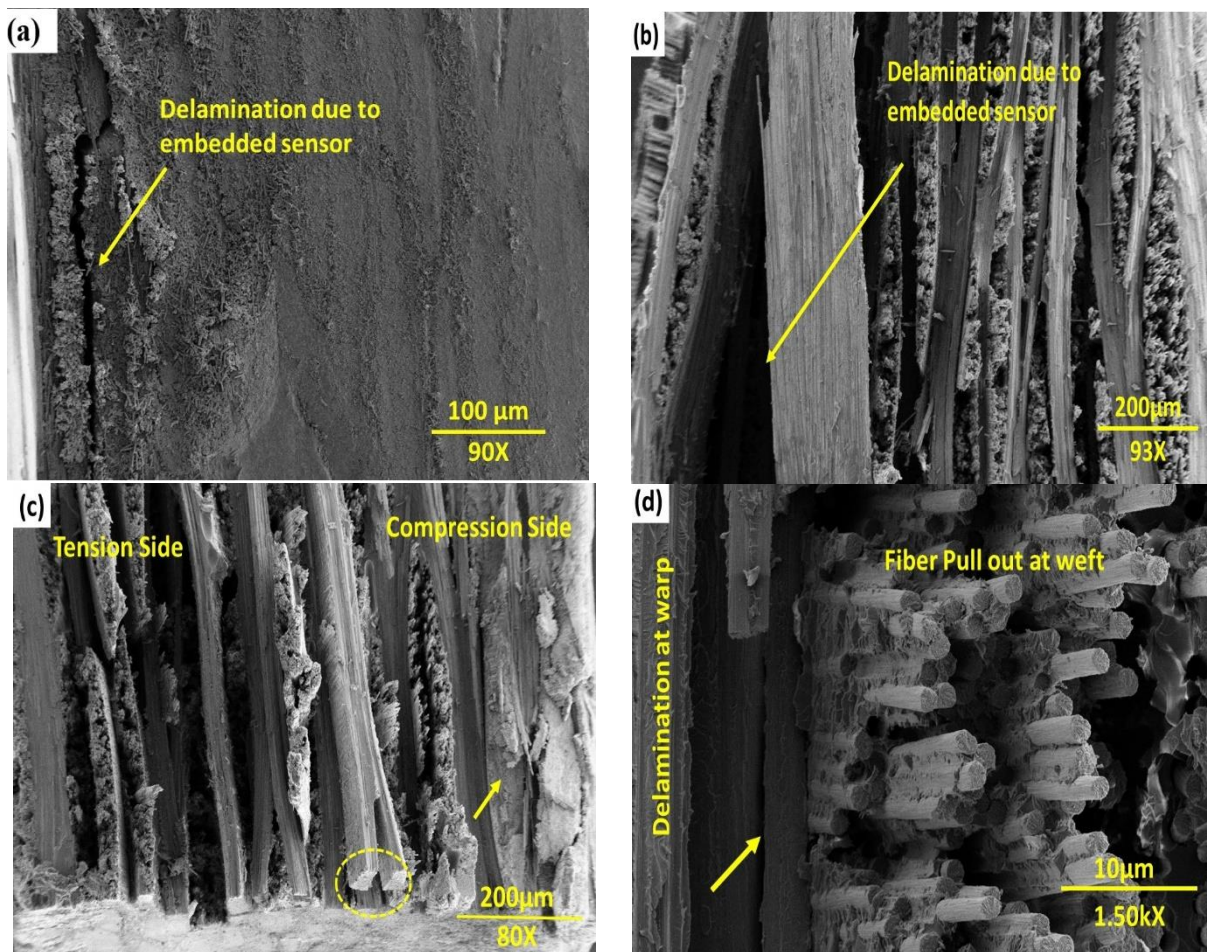


Figure 27. (a-d) Micrographs of fatigue failure for S1 and S2 where subfigure a is taken parallel to fracture surface along the width direction while the rest of the images are taken from the fracture surface.

Figure 27c presents the micrograph taken from the fracture surface of the S2 specimen with a surface mounted PVDF sensor at the compression side. It is obvious that for the surface ply in which compressive stresses are dominant, a considerable amount of fibers is crushed, hence yielding an apparent rough surface. Unlike the tension side of the specimen, the top surface shows no sign of vivid fiber pulls out nor delamination, but there is a buckling failure indicated by an arrow which has occurred due to compression at top surface ply. The bottom surface, on the other hand, depicts a considerable number of fibers pull out at weft (specimen length direction) and intralaminar damages at warp direction (specimen width direction). These failures in the bottom plies appear in an alternating pattern through the thickness. Intralaminar cracks have grown most probably in a transverse direction from the side surface of the sample; this assumption is validated by the presence of splitting at a transverse direction which has been shown in a dashed circle. Moreover, the path for crack growth under cyclic loading is stepwise and cracks have grown between weft and warp bundles through interface failure at tow regions. To better illustrate this statement, figure 27d shows SEM image of tow region, in which there is a microcrack at the vicinity of the pulled-out region indicated by an arrow. This interface microcrack indicates how the main transverse crack as delamination has propagated as a longitudinal crack at wefts direction and created the stepped fracture surface during cyclic loading. Overall, it is obvious that the delamination at warp direction is created from edges of the sample and developed inside the woven fabric laminate. The same growing cracks advance into weft bundles through interface failure which causes fiber debonding afterward. These debonding regions have then resulted in fiber breakage and pull out at the final stages of fatigue life of the sample.

CHAPTER 4

4. Static failure of composite materials

4.1. Summary

This study presents a broad analysis of the failure mechanisms in woven fabric laminates with the help of acoustic emission, DIC, and SEM. It is shown that the fracture surface of woven fabric composite laminates is directly correlated to full field strain maps of the sample at failure regions obtained through 3D-DIC. The presence of a periodic inclined region on the surface before an abrupt failure results in shear driven failure through the thickness having a smooth surface and no interlaminar delamination. On the other hand, the presence of a heterogeneous strain map with a horizontal pattern is related to the high energy required for breakage of the laminate, possessing a rough surface structure with signs of interlaminar delamination. The results of this study show that assessment of macro-strain fields at failure regions of the composite match with micro-damage obtained through SEM images, and both methods can be used as complements of one another for failure analysis of woven fabric laminates.

4.2. Experimental

4.2.1. Materials

Plain weave (KCF3KPL200) Toray T300 3K carbon fibers with an areal weight of 200gsm was purchased from Kordsa Company. BIRESIN Sika CR80 resin along with BIRESIN Sika CH80-6 hardener was utilized as a matrix. The density and viscosity values of CR80 resin were (1.13g/ml, 0.95 g/ml at 25⁰C), respectively and same for CH80-6 hardener (900m.Pa.s, <10m.Pa.s), respectively.

4.2.2. Manufacturing of composite laminate

A carbon fiber reinforced polymer composite plate with a thickness of 2mm was manufactured by using 8 layers of plain weave carbon fibers which were cut into dimensions of 30cm x 30cm with the help of a ply cutter (ZÜND G3-L3200). Biresin Sika CR 80 resin and CH80-6 hardener were mixed at the ratio of 100:30 wt/wt and degassed for 30 minutes. The fibers were stacked on a vacuum infusion table and impregnated with epoxy resin in a sealed vacuum bag and left at room temperature for 48h.

4.2.3. Mechanical testing

In order to determine tensile properties, five CFRP composite samples were prepared and tested according to ASTM D3039 using an Instron 8802 servo hydraulic testing system which is equipped with a 250kN load cell. Samples were cut into the dimensions of 25x250x2mm and bonded with

25x50x2mm CFRP composite tabs. Tensile load with the displacement of 2mm/min was applied continuously until the failure of samples. Similarly, a three-point bend test was conducted according to ASTM D790 with the help of Instron Universal Testing Machine (UTM) 5982. The fiber volume fraction and percentage void content were determined with the help of the matrix burnoff test, which was performed according to ASTM D3171. Global strain field at specimen's surface was recorded by Digital Image Correlation (DIC) using GOM (Braunschweig Germany) 12M sensor system. The blotchy pattern on the gauge length of the specimen was created by black and white paint spray. The sensor was calibrated by 250x200mm calibration plate as per the manufacturer's instructions, the results of calibration revealed 0.002mm scale deviation and 0.033pixels calibration deviation, which were both under the limit values suggested by the manufacturer. Before the initiation of the tests, surface pattern quality was inspected by ARAMIS software. The analysis was carried out with the help of GOM inspect professional software.

Acoustic emission sensors were placed on the lower surface of the three-point bending test specimen and elastic waves produced due to the development of micro damages were sensed through Acoustic Emission (AE) setup Mistras PCI-2AE, having wideband piezoelectric sensors (PICO-200-750KHz, Mistras). A preamplifier Mistras0/2/4 with the gain of 20dB was used to amplify the output signal. Data acquisition parameters for acoustic emission hardware are set to the 45db threshold, 50 μ s peak definition time, 100 μ s hit definition time and 200 μ s hit lockout time. The sampling rate of acoustic data for each sensor is set to 2MHz and a *Bessel* band-pass filter is used to remove noise from recorded data. Main features of acoustic data such as amplitude, counts, rise time are extracted from time domain waveforms, moreover, frequency domain characteristics of each acoustic hit are obtained after the Fast Fourier Transformation (FFT) analysis. The fracture surfaces of composites were examined through GEMINI SUPRA 35vp scanning electron microscope. Fractured samples were sputtered through Platinum-based sputter and images were taken at the acceleration voltage of 4kV.

4.3. Results and Discussions

4.3.1. Destructive test results

Static tests were performed to determine the stress and strain response of the composite materials. Associated mechanical properties were obtained according to ASTM D3039 and ASTM D790 for tensile and flexural tests, respectively, as seen in Table 5. The mean ultimate stress for the tensile test was 670.2MPa, while the mean failure strain value was 1.889%. Similarly, the mean flexural

strength value obtained from the three-point bending test was 711MPa while strain was 1.59%. The fiber volume fraction determined according to ASTM D-3171 was 57.63%, while void content resulted in 4.7%.

Table 5. Tensile and Three-point results.

Tensile Test		Three-point bend test	
Name of property	Mean Value	Name of property	Mean Value
Ultimate Tensile Stress (UTS)	670.2 MPa	Flexural strength	711 MPa
Strain	1.889%	Strain	1.5982%
Modulus	41.339 GPa	Modulus	50466.67 MPa
Standard deviation	32.87	Standard deviation	12.58

4.3.2. Scanning Electron Micrographs of fractured carbon fiber

SEM analysis of tensile fractured specimens provided valuable information about failure modes such as delamination, shear imprints, and fiber breakage. Figure 28(a) shows a cross-section of weft fibers in the axial direction. The surface of failure was smooth which indicated brittle fracture progress due to sudden propagation of a crack normal to the loading direction. The presence of fiber pullouts in the same region implies that the high energy required for this damage type had hindered the fast crack growth.

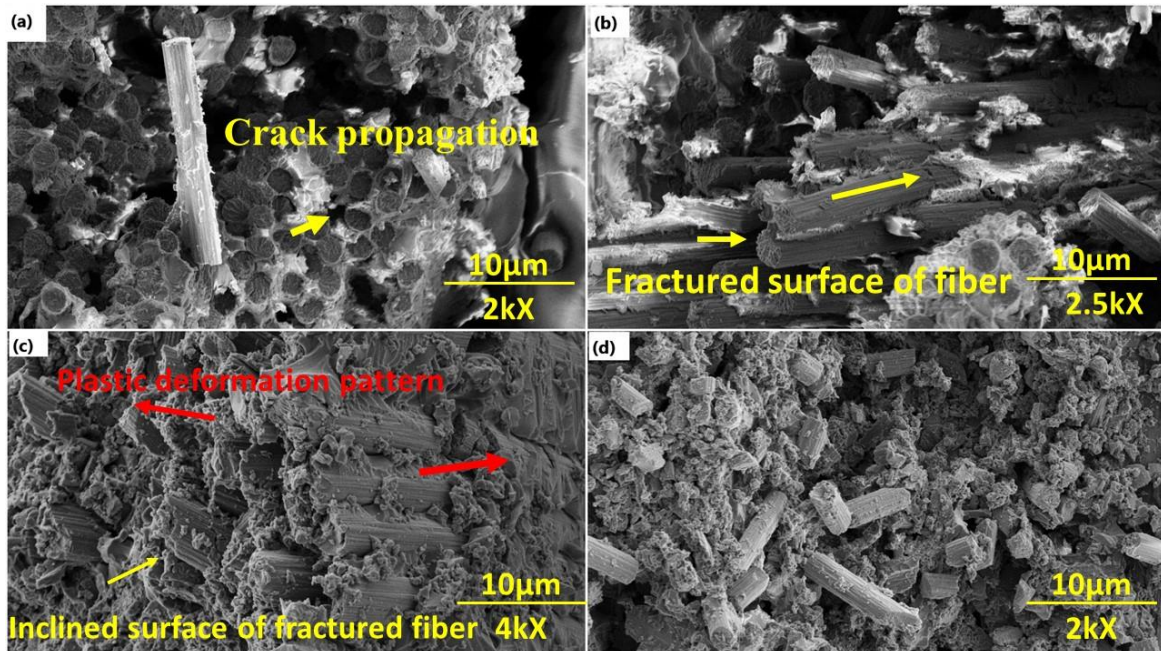


Figure 28. SEM micrographs of carbon fibers from failure regions of composites. (a) & (b) rupture dominant region; (c) & (d) shear dominant region.

On the other hand, figure 28b illustrates the cohesive interfacial failure between warp fibers and the matrix, wherein the fibers were in a lateral direction with respect to the loading axis. A very small amount of matrix debris observed on debonded fibers indicates slow debonding as the cracks grew. Despite the neat surfaces of these warp fibers, their cross-section was rough compared to those in Figure a which signifies breakage of these fibers as a response to a bending moment. The effect of this bending force shown by a yellow arrow in the figure 28b as it broke a fiber just at the point where debonding has stopped. Overall, it is evident that the matrix had been completely debonded due to crack growth and did not support the fibers in the warp direction, which is why there was very little matrix debris visible on the surface of the fibers.

Figure 28c shows the cross-section of the same failed sample at a different region. The presence of the matrix on the surface of the failed fibers suggested that the failure was adhesive, which means that the fibers had strong interfacial bonding with the matrix and more energy was required for crack growth in this region. The presence of plastic deformation patterns at the matrix surface (red arrow) shows energy absorption by the matrix during the crack propagation procedure. The surface of fibers in figure 28c is rough but they are inclined with respect to their fiber axis. This type of fiber failure indicates shear fracture mode for the fibers. Overall, the shear stresses had been the dominant failure development promoters both in matrix and fibers.

Figure 28d represents the failure area of weft fibers broken in the direction of loading in the shear dominant regions. It depicts the fiber pullout and angled surface of fractured fibers, which suggests the presence of shear stresses. The presence of a rough surface at the matrix is evidence that high energy was absorbed during the failure development by the epoxy resin matrix.

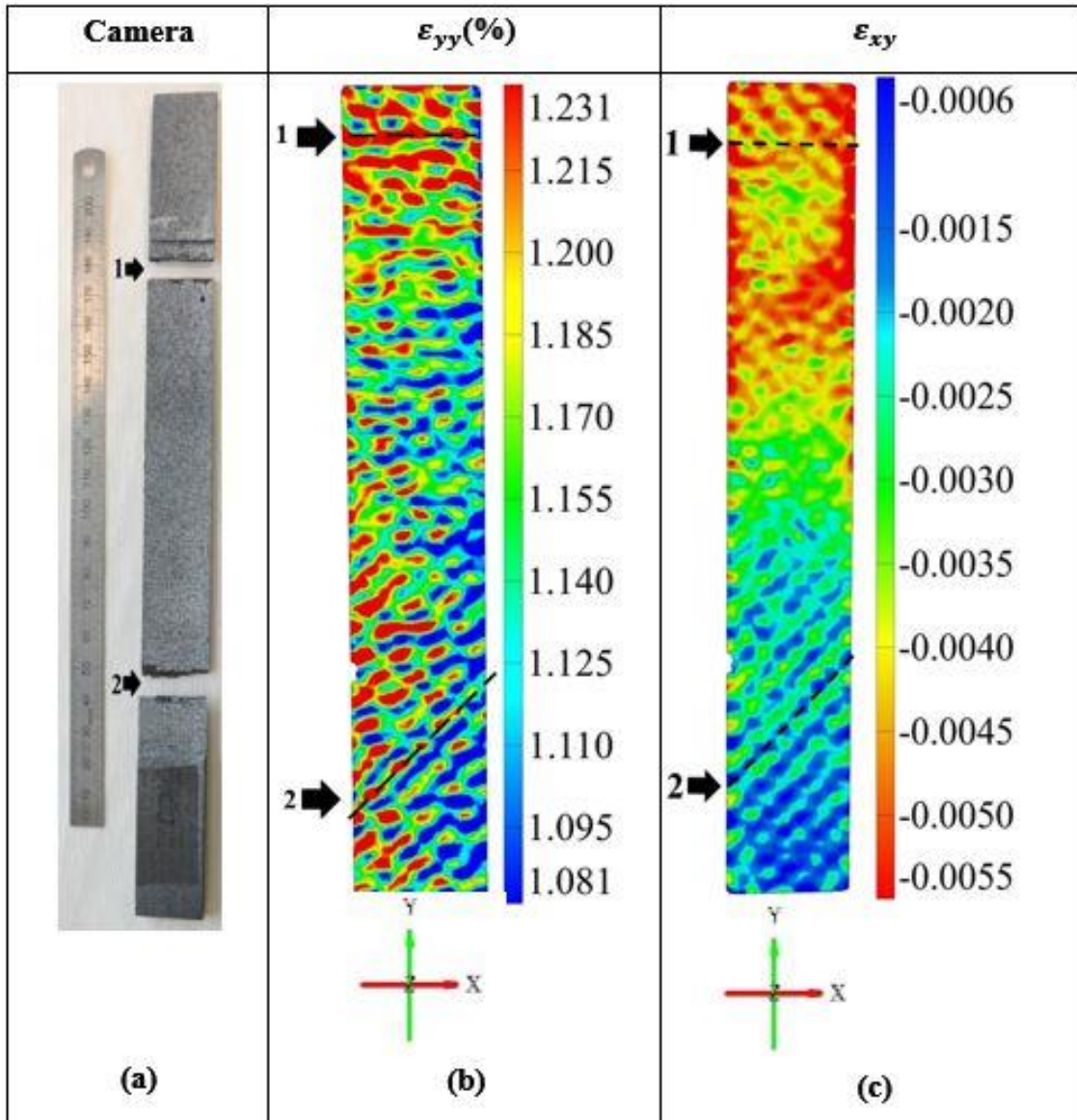
To classify the mechanism of failure in the shear dominant and rupture dominant regions, it can be stated that for adhesive failure, the matrix showed a rough texture with residues of the matrix on the fibers. Moreover, the fibers had a rough and inclined cross section due to the presence of shear stresses. On the other hand, rupture dominant failures produced a neat fiber surface in the weft direction and rough cross-section in the warp direction. From these observations, one can be seen that various stress types correspond to different failure modes in fibers and the amount of the energy required for failure development in a specific region can be obtained through the marks left on matrix material after fracture of the composite sample.

4.3.3. Full-field strain measurements as an indicator of failure mechanisms

Figure 29a shows an image of the broken tensile sample, which demonstrated transverse failure at two regions far apart, indicated as regions R1 and R2. Although these failure regions might seem to have a similar macroscopic appearance, their DIC images taken just before the abrupt failure stage revealed differences between their strain fields, therefore indicating distinct mechanisms involved in the fracture of each region. Figure 29b depicts the vertical strain (ϵ_{yy}) map for the fractured sample, in which the longitudinal strains varied from 1.08% to 1.231%. The heterogeneous distribution of strain throughout the gauge length was due to the variation of the elastic modulus of fibers and the matrix, hence producing low strain at tow regions and high strain at adjacent resin packet regions. The important thing to notice is that the lower half of specimen, i.e. failure region R2, shows periodically inclined (dashed line) deformation, and this strip shaped deformation pattern, continues up to the middle region of the gauge length. The middle region does not show any regular pattern while the top area of the sample shows some transverse stripes just normal to the loading direction, that is, the failure region R1. These arrangements of deformation at various locations of the specimen clearly show the dominance of different stress fields; therefore, shear driven, and longitudinally normal stresses will control the fracture of the sample at R2 and R1, respectively. To illustrate the overriding effect of shear stresses at failure region R2. Figure 29c shows the full field shear strain map of the laminate. It can be seen that the striped pattern of shear strain has a gradient between -0.0006 and -0.003, indicating a change of almost five times in shear deformation values. However, the shear strain field for the upper region, i.e. R1, has a gradient between -0.0055 and -0.003, which is about 1.5 times. Thus, the full field measurement of shear strains signifies the presence of considerable shear stress at the lower part of the sample.

To determine the results of such different strain fields on fracture appearance in micro scale, SEM images from cross sections of each region are presented in figure 29d & e. These images are taken from the right edge, center and the left edge of the fracture cross section and are represented as top, center and bottom figures respectively. As seen in figure 29d, the fracture surface shows a very rough surface with delamination marks and fiber pullouts through the cross-section. Both failure types require friction; in other words, a rough surface indicates the high energy required for failure development, which is more probable under a pure tensile stress condition, therefore demonstrating consistency with the longitudinal strain field in the upper half of the specimen seen

in the DIC images. On the other hand, figure 29e shows a smoother surface, which is a characteristic of low energy fracture with very few signs of interlaminar failures and fiber pullouts. This surface shows various regions with cusp and fiber imprints, indicating the shear dominant development of damage. These surface images of fracture are also in agreement with the DIC images obtained from the surface of the material in that region, i.e. vivid shear strain fields and small vertical strain gradients.



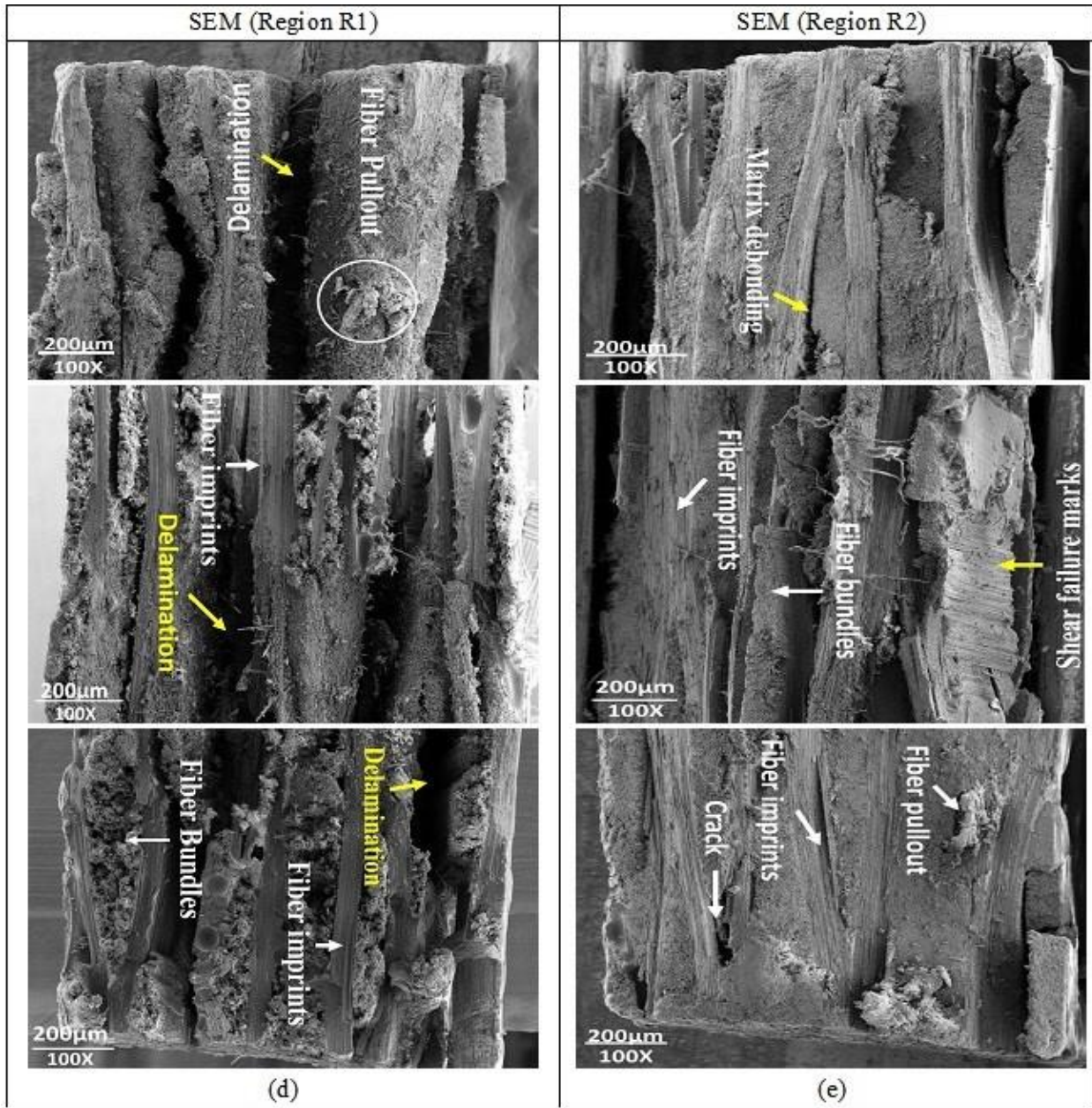


Figure 29. Failure of composites (a) broken sample; (b) & (c) strain map of ϵ_{yy} , ϵ_{xy} ; (d) & (e) SEM images of fractured surfaces of the composite.

4.3.4. Acoustic emission analysis

Weighted Peak Frequency and Partial Power 1 features of acoustic hits are used to cluster acoustic emission data. These features have demonstrated excellent clustering results in the previous investigation for composite materials [35]. Weighted Peak frequency is a function of frequency centroid and peak frequency of the frequency domain which is a representation of acoustic hits.

Frequency centroid ($f_{centroid}$) is defined as an analogous to the center of mass in the frequency spectrum, while peak frequency (f_{peak}) is the frequency value with the highest magnitude in the same range. As seen in Eq. (5), Frequency centroid is calculated through a weighted mean formula as shown in Eq. (6), in which the magnitude $M(s)$ of each frequency (s) is used as weight. The partial a power concept is defined by the user for certain frequency ranges to find the percentage of the power spectrum located in that frequency range; therefore, partial powers are reported as percentages. Table 6 represents the range of partial powers defined for the clustering of acoustic hits in this investigation:

$$f_{centroid} = \sum_{s=0}^{s=1000} f(s)M(s) / \sum_{s=0}^{s=1000} M(s) \quad \text{Equation 5}$$

$$\text{Weighted Peak frequency (WPF)} = \sqrt{f_{centroid} \times f_{peak}} \quad \text{Equation 6}$$

Table 6. Frequency ranges

Partial Power 1	0 – 250 KHz
Partial Power 2	250 – 500kHz
Partial Power 3	500 – 750kHz
Partial Power 4	750 – 1000kHz

To determine the optimal number of clusters for implementation of the clustering algorithm, the *GAP* evaluation function is used as a global procedure, which is remarkable for the elongated distribution of a data point, as seen in figure 30b. This function finds an error value (w_k) for the various numbers of clusters obtained through the clustering algorithm, indicating the optimal number of clusters as the point where *GAP* function is maximum. *GAP* value is defined as Eq. 7:

$$GAP_n(k) = E_n^*\{\log(w_k)\} - \log(w_k) \quad \text{Equation 7}$$

Where n is the size of a sample taken from the data, k is the number of clusters that are being evaluated, $E_n^*\{\log(w_k)\}$ denotes expectation taken from a reference sample using the Monte Carlo method, and w_k is composite variance inside the cluster sum of squares[38].

4.3.5. Clustering Results

Figure 30a represents the obtained acoustic emission data for B1 laminate under flexural loading before the implementation of the clustering algorithm. Based on this distribution of acoustic data it is highly important to estimate the precise value for cluster numbers since there is no distinct definition of the cluster for these data and process is unsupervised. Since the obtained acoustic data is elongated, we use *GAP* value to find the optimal number of clusters. Figure 30b shows the results of *GAP* evaluation for the B1 sample with the K-means algorithm. Since common failures in composite laminates can be classified in 5 main types, namely matrix cracking, debonding, delamination, fiber pull out and fiber breakage, the evaluation is depicted for 1 up to 5 cluster numbers. However, it is seen that the maximum point of the *GAP* value, i.e. the optimal number of clusters is 3, which provides the best separation between the clusters, and it is inferred that three damage types are signified. These 3 types of failure can be extracted from the mentioned categories of damage considering that debonding and delamination are both interface failures, and that fiber pullout is not very frequent under three-point bending conditions. In other words, damage modes can be reduced to matrix cracking, interface failure, and fiber breakage.

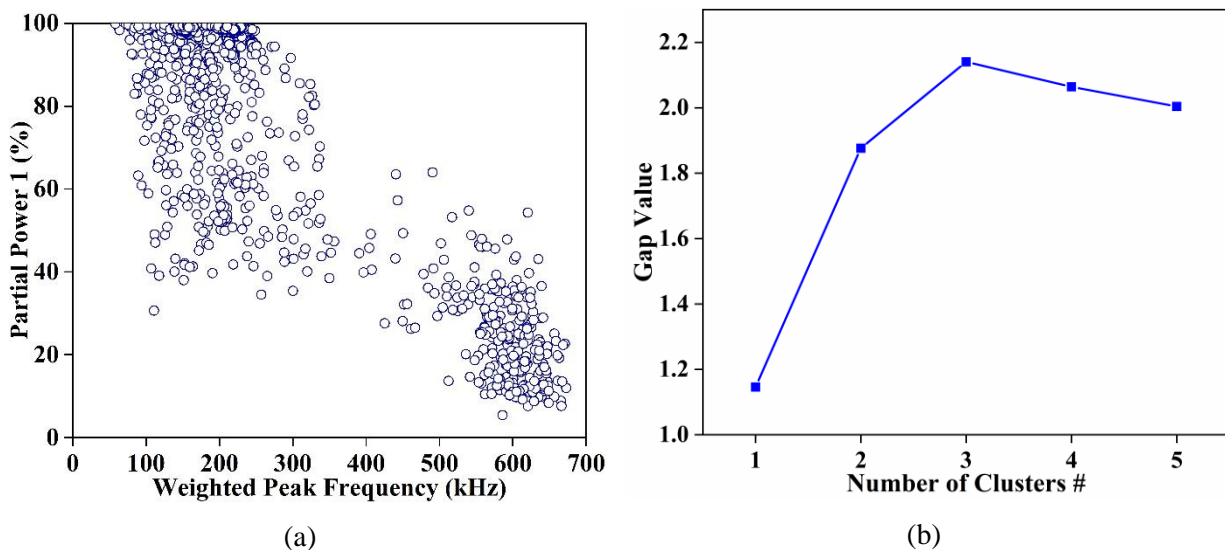


Figure 30. (a) Acoustic emission results for flexural test; (b) Gap values obtained for each cluster numbers.

After selection of the optimum number of clusters, the K-means function of MATLAB software with Euclidean distance parameter is used to identify 3 clusters of acoustic emission data for each laminate under flexural loading. The results of the K-means algorithm based on Weighted Peak

frequency and Partial Power 1 are seen in figure 31. Three distinctive clusters are seen at three different frequency ranges, 50-180 kHz, 180-400 kHz, and 400-670kHz. According to the previous investigation by the authors, the lowest frequency range of acoustic emission activity corresponds to damage inside low stiffness matrix material [34]. Moreover, the highest frequency events are attributed to fiber breakage, and the middle range of acoustic emission data points is due to the failure of the interface between fiber and matrix. Since the partial power 1 frequency range is 0-250 kHz, it can be inferred from clustering results that more than 50% of the power in matrix cracking and interface failure is located at low frequencies, while for fiber breakage the power is mainly located at higher frequencies. Therefore, it can be concluded that higher stiffness of materials would possess the main fraction of their power at higher frequency ranges.

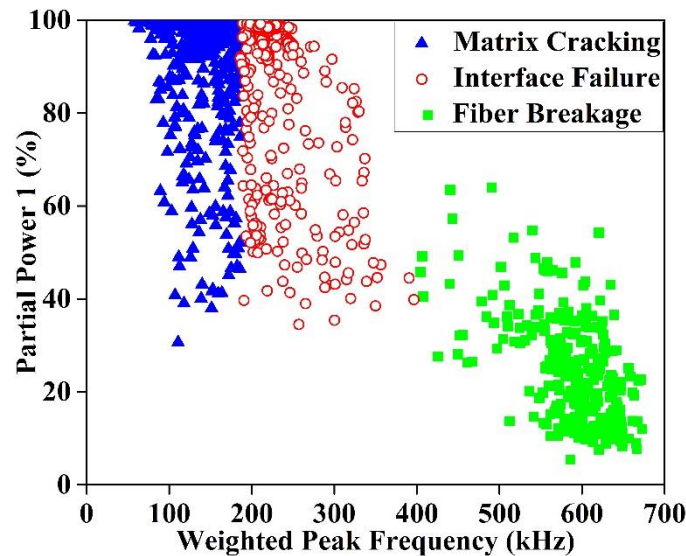


Figure 31. Clustering results for specimen under flexural loading.

4.3.6. Damage accumulation analysis based on AE activity

Figure 32(a&b) show the acoustic emission activity of B1 and B2 samples merged with the stress-strain curve under flexural loading test. These two samples represent two categories of failed specimens which were classified based on first damage which appeared during the flexural test. The first damage to appear in the B1 sample was fiber breakage, while initial failure occurrence in the B2 specimen was related to interface damage. Despite the incidence of damage at early stages of flexural loading, no considerable effect was seen in the stiffness of materials, i.e. the slope of the stress-strain curve. To better analyze the change in stiffness of each laminate, a line is fitted in strains between 0.002 to 0.006 ϵ for each laminate. As seen in figure 32a, despite the occurrence

of several fiber breakages at the 0.009 ϵ strain level, no deviation is seen between the linear fitting and experimental results. Only at a strain level of about 0.011 ϵ , shown as region **I**, deviation starts from linear behavior, which corresponds to the simultaneous failure of the matrix, failures at fibers, and interface damages. These results suggest that sole failure at fiber, i.e. damage with the highest weighted peak frequency, cannot influence the stiffness of woven fabric laminates significantly.

Figure 32b depicts that the behavior of the B2 specimen was different. The first failure to occur for this laminate was interface failure at about 0.003 strain level, and yet no distinguishable effect is seen in the stress-strain behavior of the sample. It is clearly seen that this sample shows a sudden increase in acoustic emission activity at 0.09 strain indicated by region **I**, similar to the B1 laminate represented in figure 32a. However, the difference is that the type of damage is interface failure, which causes a vivid deviation from linear stress-strain behavior. Based on this observation, it can be stated that interface failures with a weighted peak frequency range of 180-400 kHz have a significant impact on the mechanical behavior of woven carbon fiber laminates compared to fiber breakages. Therefore, reinforcer material in woven fabric laminates does not necessarily provide flexural stiffness during bending tests figure 32b also shows a hump at about a strain level of 0.012, indicated as region **II**, which corresponds directly to the concurrent failure of the matrix, failure of fibers, and interfaces damages. Similar to the previous specimen, the main change in material behavior happens when all failure types are triggered together. This observation signifies that major failures including all types of damage are the prominent causes for the loss of stiffness under flexural loading.

Overall, it is seen that two types of failure can happen at the beginning of flexural loading for woven carbon fabric laminates, namely fiber breakage and interface failure. These failures have no meaningful impact on the structural health of materials, most probably due to their small size and/or quantity. Both samples show a sudden increase in energy of damage at around 0.009 strain. This upsurge of failure energy changes stress-strain behavior and corresponds to the initiation of major failures inside the laminate. It should be noted that if a sudden increase in energy is related to interface failure, then it alters the modulus of the material, but still, it is not critical. The crucial change in the stiffness of laminates happens only if all damage types occur concurrently and they cause deviation from linear behavior in the stress-strain curve.

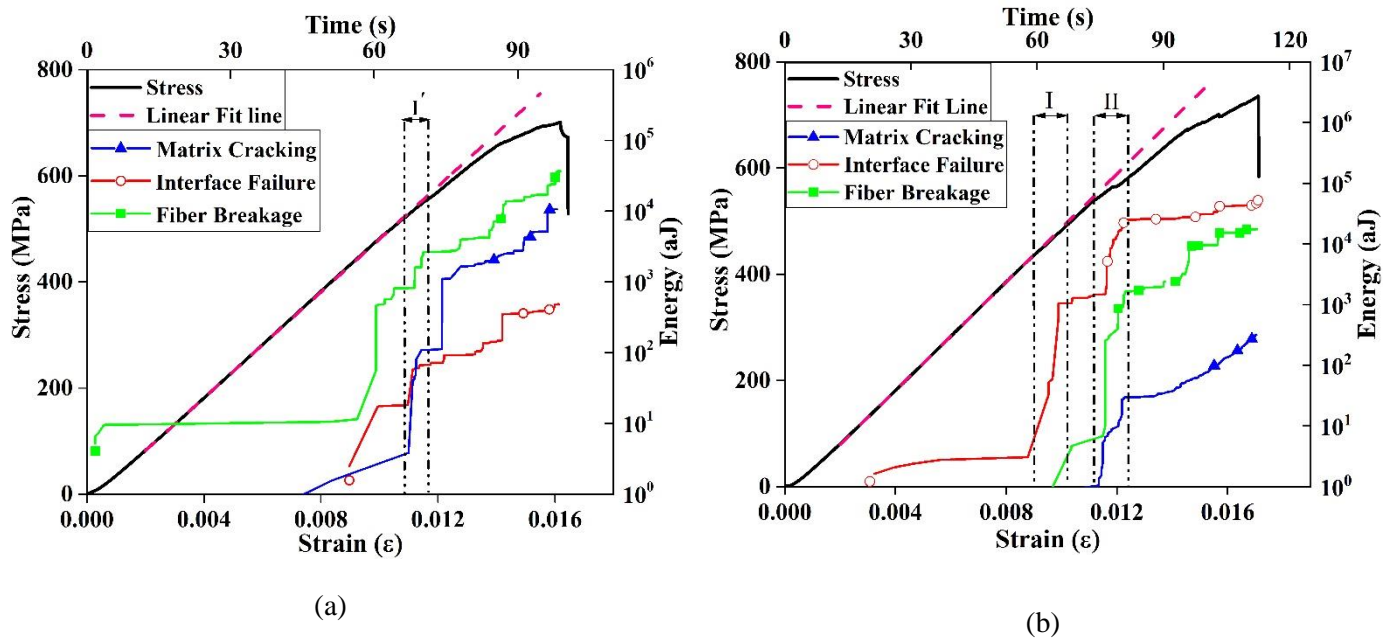


Figure 32. Flexural strength and energy versus strain and time for a) B1 b) B2

4.3.7. SEM Analysis of failed specimens under flexural loading

Figure 33a shows a cross-section of the failure region for specimen B1. The appearance of the fracture surface changes vividly from a uniform and squashed configuration at the compressive side to a more rough and jagged layout at the tension side of the sample. The vertical dashed line at the middle of figure 33a distinguishes between these two regions and can be considered as the midplane for the neutral axis under flexural loading. As seen in figure 33b, at tensile half of the sample, broken fibers of the weft direction show signs of uneven fiber pull out, whereas, for weft fibers at the compressive side, buckled fibers and an even surface are observed, as seen in figure 33c. All these fiber failures types, i.e. broken, pulled out and/or crushed, correspond to the AE signals with weighted peak frequencies between 400-670kHz. The fibers in the warp direction of the sample, as seen in figure 33b, show severe intralaminar delamination and interface failures (fiber imprints), which are attributed to AE hits with a weighted peak frequency range between 180-400 kHz. It is seen that all three types of failure associated with AE data can be found in SEM images of broken flexural tested samples, therefore confirming the reliability of the clustering result for AE signals.

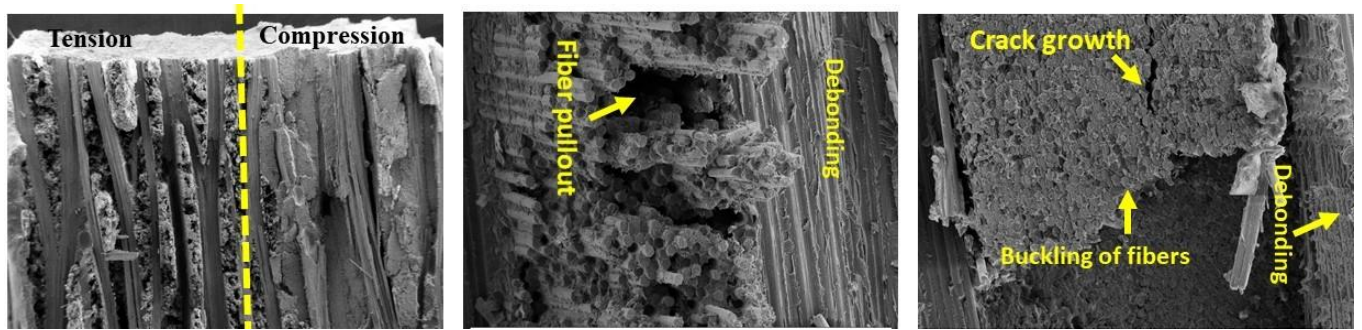


Figure 33. SEM images of fractured surfaces of the composite under three-point bend loading

CHAPTER 5

5. Conclusion

Electrospun nanofibers have a dominant active phase (β -phase) as compared to raw PVDF granule which has a higher content of non-active phase (α -phase). The FTIR results also confirm that electrospun nanofibers have a 46% higher β -phase content contrast to granule. Contrary to PVDF granule the PVDF nanofibers have 25% higher crystallinity without any notable effect on melting temperature. In XRD analysis, PVDF nanofibers have a significant peak of β -phase while PVDF granule spectrum has a prominent α -phase peak and a low-intensity β -phase peak. SEM images of PVDF nanofibers also assure the quality of produced fibers. Fibers having a diameter in the range of 30 to 90nm, produced through the electrospinning process, do not show any significant sign of porosity and beads formation.

Embedding sensor inside the structure can be problematic for its fatigue life as it promotes delamination while the surface attached sensor has better fatigue performance. PVDF sensor has the capability to detect the variation in the specimen as a response of the applied load. Although PVDF sensors have some drawbacks due to backlash and resistance of electrode materials, which reduces their output voltage, they are still a good thin and flexible replacement for conventional strain gauges thin. PVDF films have the capability to be utilized as a sensor to monitor the loading history and damage progression in structures without any external power excitation which is confirmed by its usage in fatigue testing. However, these sensors need to be calibrated to determine the correlation between the strain or load and output voltage.

Overall for continuous monitoring of aircraft and giant composite structures where numerous sensors are required for testing, these flexible PVDF sensors are the reliable and durable option which can provide an adequate solution for dynamic strain monitoring and structural health monitoring.

A more detailed analysis of fracture surfaces for tensile samples reveals that despite the smooth appearance of surface failure in shear dominant regions, the matrix has a rough texture, and debris of the matrix can also be observed on the surface of fibers. Furthermore, fibers broken due to the shear have an inclined cross-section and harsh texture. In the case of the region with normal stress fields, detailed analysis of the fracture area shows smooth fiber surface with little matrix debris and a rough cross-section along with plane matrix.

For the first time, the *GAP* evaluation function is successfully used to find the optimal number of clusters before applying the K-means algorithm on acoustic emission data of the three-point bending test. This evaluation reveals 3 clusters as the optimal number to classify damage types under flexural loading. The three distinct failure types for woven carbon fabric laminates under bending test condition are matrix cracking, interface failure, and fiber breakage, which possesses weighted peak frequency range of 50-180 kHz, 180-400 kHz, and 400-670kHz respectively. Acoustic emission analysis which is used to determine damage accumulation under flexural loading shows that major change in stiffness of woven laminates is attributed to simultaneous occurrence matrix, fiber, and interface failures. No significant change in material integrity occurs if a single type of failure happens at the early stages of the bending test. SEM analysis of failed regions for flexural samples reveals that all failure types classified through acoustic emission are present in microscopic analysis and microscopic inspection can be used to certify the results of acoustic emission pattern recognition procedure.

References

1. Singh, D., Choudhary, A., Garg, A.: Flexible and Robust Piezoelectric Polymer Nanocomposites Based Energy Harvesters. *ACS applied materials & interfaces*. 10, 2793–2800 (2018)
2. Ueberschlag, P.: PVDF piezoelectric polymer. *Sensor review*. 21, 118–126 (2001)
3. Richards, C.D., Anderson, M.J., Bahr, D.F., Richards, R.F.: Efficiency of energy conversion for devices containing a piezoelectric component. *Journal of Micromechanics and Microengineering*. 14, 717 (2004)
4. Chang, J., Dommer, M., Chang, C., Lin, L.: Piezoelectric nanofibers for energy scavenging applications. *Nano energy*. 1, 356–371 (2012)
5. Bachmann, M.A., Gordon, W.L., Koenig, J.L., Lando, J.B.: An infrared study of phase-III poly (vinylidene fluoride). *Journal of Applied Physics*. 50, 6106–6112 (1979)
6. Lund, A., Hagström, B.: Melt spinning of poly (vinylidene fluoride) fibers and the influence of spinning parameters on β -phase crystallinity. *Journal of applied polymer science*. 116, 2685–2693 (2010)
7. Chiu, F.-C., Chen, Y.-J.: Evaluation of thermal, mechanical, and electrical properties of PVDF/GNP binary and PVDF/PMMA/GNP ternary nanocomposites. *Composites Part A: Applied Science and Manufacturing*. 68, 62–71 (2015). doi:<https://doi.org/10.1016/j.compositesa.2014.09.019>
8. Sessler, G.M.: Piezoelectricity in polyvinylidene fluoride. *The Journal of the Acoustical Society of America*. 70, 1596–1608 (1981)
9. Weinhold, S., Litt, M.H., Lando, J.B.: The Crystal Structure of the γ Phase of Poly(vinylidene fluoride). *Macromolecules*. 13, 1178–1183 (1980). doi:[10.1021/ma60077a029](https://doi.org/10.1021/ma60077a029)
10. Martins, P., Lopes, A.C., Lanceros-Mendez, S.: Electroactive phases of poly (vinylidene fluoride): determination, processing and applications. *Progress in polymer science*. 39, 683–706 (2014)
11. Seyyed Monfared Zanjani, J., Saner Okan, B., Yilmaz, C., Menciloglu, Y., Yildiz, M.: Monitoring the interface and bulk self-healing capability of tri-axial electrospun fibers in glass fiber reinforced epoxy composites. *Composites Part A: Applied Science and Manufacturing*. 99, 221–232 (2017). doi:<https://doi.org/10.1016/j.compositesa.2017.04.017>
12. Fang, J., Niu, H., Lin, T., Wang, X.: Applications of electrospun nanofibers. *Chinese science bulletin*. 53, 2265 (2008)
13. Fang, J., Wang, X., Lin, T.: Electrical power generator from randomly oriented electrospun poly (vinylidene fluoride) nanofibre membranes. *Journal of Materials Chemistry*. 21, 11088–11091 (2011)
14. Sengupta, D., Kottapalli, A.G.P., Chen, S.H., Miao, J.M., Kwok, C.Y., Triantafyllou, M.S., Warkiani, M.E., Asadnia, M.: Characterization of single polyvinylidene fluoride

- (PVDF) nanofiber for flow sensing applications. *AIP Advances*. 7, 105205 (2017)
15. Diamanti, K., Soutis, C.: Structural health monitoring techniques for aircraft composite structures. *Progress in Aerospace Sciences*. 46, 342–352 (2010). doi:<https://doi.org/10.1016/j.paerosci.2010.05.001>
 16. Schubel, P.J., Crossley, R.J., Boateng, E.K.G., Hutchinson, J.R.: Review of structural health and cure monitoring techniques for large wind turbine blades. *Renewable Energy*. 51, 113–123 (2013). doi:<https://doi.org/10.1016/j.renene.2012.08.072>
 17. Le, M.Q., Capsal, J.-F., Lallart, M., Hebrard, Y., Van Der Ham, A., Reffe, N., Geynet, L., Cottinet, P.-J.: Review on energy harvesting for structural health monitoring in aeronautical applications. *Progress in Aerospace Sciences*. 79, 147–157 (2015). doi:<https://doi.org/10.1016/j.paerosci.2015.10.001>
 18. Akay, E., Yilmaz, C., Kocaman, S.E., Turkmen, S.H., Yildiz, M.: Monitoring Poisson's Ratio Degradation of FRP Composites under Fatigue Loading Using Biaxially Embedded FBG Sensors, <https://www.mdpi.com/1996-1944/9/9/781/htm>, (2016)
 19. Shin, Y.-H., Jung, I., Park, H., Pyeon, J., Son, J., Koo, C., Kim, S., Kang, C.-Y.: Mechanical Fatigue Resistance of Piezoelectric PVDF Polymers. *Micromachines*. 9, 503 (2018)
 20. Hofmann, P., Walch, A., Dinkelmann, A., Selvarayan, S.K., Gresser, G.T.: Woven piezoelectric sensors as part of the textile reinforcement of fiber reinforced plastics. *Composites Part A: Applied Science and Manufacturing*. 116, 79–86 (2019). doi:<https://doi.org/10.1016/j.compositesa.2018.10.019>
 21. Zhang, Y.: In situ fatigue crack detection using piezoelectric paint sensor. *Journal of Intelligent Material Systems and Structures*. 17, 843–852 (2006)
 22. Gama, A.L., Morikawa, S.R.K.: Monitoring Fatigue Crack Growth in Compact Tension Specimens Using Piezoelectric Sensors. *Experimental Mechanics*. 48, 247–252 (2008). doi:[10.1007/s11340-007-9086-0](https://doi.org/10.1007/s11340-007-9086-0)
 23. De, M., Pozegic, T., Hamerton, I., Fotouhi, M.: Development and evaluation of a novel piezoelectric PVDF sensor as a load spectrum counter. (2018)
 24. Ihn, J.-B., Chang, F.-K.: Detection and monitoring of hidden fatigue crack growth using a built-in piezoelectric sensor/actuator network: I. Diagnostics. *Smart materials and structures*. 13, 609 (2004)
 25. Tuloup, C., Harizi, W., Aboura, Z., Meyer, Y., Khellil, K., Lachat, R.: On the use of in-situ piezoelectric sensors for the manufacturing and structural health monitoring of polymer-matrix composites: A literature review. *Composite Structures*. 215, 127–149 (2019). doi:<https://doi.org/10.1016/j.compstruct.2019.02.046>
 26. Zhao, X., Gao, H., Zhang, G., Ayhan, B., Yan, F., Kwan, C., Rose, J.L.: Active health monitoring of an aircraft wing with embedded piezoelectric sensor/actuator network: I. Defect detection, localization and growth monitoring. *Smart materials and structures*. 16, 1208 (2007)

27. Sirohi, J., Chopra, I.: Fundamental understanding of piezoelectric strain sensors. *Journal of intelligent material systems and structures*. 11, 246–257 (2000)
28. Jung, I., Shin, Y.-H., Kim, S., Choi, J., Kang, C.-Y.: Flexible piezoelectric polymer-based energy harvesting system for roadway applications. *Applied energy*. 197, 222–229 (2017)
29. Garcia, C., Trendafilova, I.: Triboelectric sensor as a dual system for impact monitoring and prediction of the damage in composite structures. *Nano Energy*. (2019)
30. Gutiérrez, N.A.C. and E.: Evaluation of the sensitivity and fatigue performance of embedded piezopolymer sensor systems in sandwich composite laminates. *Smart Materials and Structures*. 24, 25032 (2015)
31. Ivanov, D.S., Lomov, S. V, Bogdanovich, A.E., Karahan, M., Verpoest, I.: A comparative study of tensile properties of non-crimp 3D orthogonal weave and multi-layer plain weave E-glass composites. Part 2: Comprehensive experimental results. *Composites Part A: Applied Science and Manufacturing*. 40, 1144–1157 (2009). doi:<https://doi.org/10.1016/j.compositesa.2009.04.032>
32. Lomov, S. V, Ivanov, D.S., Truong, T.C., Verpoest, I., Baudry, F., Vanden Bosche, K., Xie, H.: Experimental methodology of study of damage initiation and development in textile composites in uniaxial tensile test. *Composites Science and Technology*. 68, 2340–2349 (2008). doi:<https://doi.org/10.1016/j.compscitech.2007.07.005>
33. Paipetis, A.S.: Damage Assessment in Fibrous Composites Using Acoustic Emission. Presented at the (2012)
34. Yilmaz, C., Akalin, C., Gunal, I., Celik, H., Buyuk, M., Suleman, A., Yildiz, M.: A hybrid damage assessment for E-and S-glass reinforced laminated composite structures under in-plane shear loading. *Composite Structures*. 186, 347–354 (2018). doi:<https://doi.org/10.1016/j.compstruct.2017.12.023>
35. Sause, M.G.R., Gribov, A., Unwin, A.R., Horn, S.: Pattern recognition approach to identify natural clusters of acoustic emission signals. *Pattern Recognition Letters*. 33, 17–23 (2012). doi:<https://doi.org/10.1016/j.patrec.2011.09.018>
36. Li, L., Lomov, S. V, Yan, X., Carvelli, V.: Cluster analysis of acoustic emission signals for 2D and 3D woven glass/epoxy composites. *Composite Structures*. 116, 286–299 (2014). doi:<https://doi.org/10.1016/j.compstruct.2014.05.023>
37. Bohmann, T., Schlamp, M., Ehrlich, I.: Acoustic emission of material damages in glass fibre-reinforced plastics. *Composites Part B: Engineering*. 155, 444–451 (2018). doi:<https://doi.org/10.1016/j.compositesb.2018.09.018>
38. Tibshirani, R., Walther, G., Hastie, T.: Estimating the number of clusters in a data set via the gap statistic. *Journal of the Royal Statistical Society: Series B (Statistical Methodology)*. 63, 411–423 (2001)
39. Gao, F., Boniface, L., Ogin, S.L., Smith, P.A., Greaves, R.P.: Damage accumulation in woven-fabric CFRP laminates under tensile loading: Part 1. Observations of damage accumulation. *Composites science and technology*. 59, 123–136 (1999)

40. Loutas, T.H., Kostopoulos, V.: Health monitoring of carbon/carbon, woven reinforced composites. Damage assessment by using advanced signal processing techniques. Part I: Acoustic emission monitoring and damage mechanisms evolution. *Composites science and technology*. 69, 265–272 (2009)
41. Nag-Chowdhury, S., Bellégou, H., Pillin, I., Castro, M., Longrais, P., Feller, J.F.: Crossed investigation of damage in composites with embedded quantum resistive strain sensors (sQRS), acoustic emission (AE) and digital image correlation (DIC). *Composites Science and Technology*. 160, 79–85 (2018)
42. Sutton, M.A., Orteu, J.J., Schreier, H.: Image correlation for shape, motion and deformation measurements: basic concepts, theory and applications. Springer Science & Business Media (2009)
43. Tang, J., Zhou, G., Wang, X., Li, C., Silberschmidt, V. V: Failure analysis of plain woven glass/epoxy laminates: Comparison of off-axis and biaxial tension loadings. *Polymer Testing*. 60, 307–320 (2017)
44. Nicoletto, G., Anzelotti, G., Riva, E.: Mesoscopic strain fields in woven composites: experiments vs. finite element modeling. *Optics and Lasers in Engineering*. 47, 352–359 (2009)
45. Koohbor, B., Ravindran, S., Kidane, A.: Meso-scale strain localization and failure response of an orthotropic woven glass–fiber reinforced composite. *Composites Part B: Engineering*. 78, 308–318 (2015). doi:<https://doi.org/10.1016/j.compositesb.2015.03.064>
46. Boufaïda, Z., Boisse, J., André, S., Farge, L.: Mesoscopic strain field analysis in a woven composite using a spectral solver and 3D-DIC measurements. *Composite Structures*. 160, 604–612 (2017)
47. Rokbi, M., Osmani, H., Benseddiq, N., Imad, A.: On experimental investigation of failure process of woven-fabric composites. *Composites Science and Technology*. 71, 1375–1384 (2011)
48. Mayén, J., Abúndez, A., Alcudia, E., Arellano, J.A., Colín, J., Pereyra, I., Puente-Lee, I.: Fractographic relation between progressive failure and strain measurement techniques for recently developed configuration of carbon fiber/epoxy laminate. *Polymer Testing*. 57, 156–164 (2017)
49. Dixit, A., Mali, H.S., Misra, R.K.: Investigation of the thermomechanical behavior of a 2×2 twill weave fabric advanced textile composite. *Mechanics of Composite Materials*. 51, 253–264 (2015)
50. Greenhalgh, E., Hiley, M.: Fractography of polymer composites: current status and future issues. (2008)
51. Kumar, M.S., Raghavendra, K., Venkataswamy, M.A., Ramachandra, H.V.: Fractographic analysis of tensile failures of aerospace grade composites. *Materials Research*. 15, 990–997 (2012)
52. Seminara, L., Capurro, M., Cirillo, P., Cannata, G., Valle, M.: Electromechanical characterization of piezoelectric PVDF polymer films for tactile sensors in robotics

- applications. *Sensors and Actuators A: Physical*. 169, 49–58 (2011)
53. Conformal Piezoelectric Mechanical Energy Harvesters: Mechanically Invisible Human Dynamos, <https://www.media.mit.edu/projects/conformal-piezoelectric-mechanical-energy-harvesters/overview/>
 54. Flexible piezoelectric devices for gastrointestinal motility sensing, <https://www.media.mit.edu/projects/lead-zirconate-titanate-gastrointestinal-sensor-pzt-gis/overview/>
 55. Zhuang, Y.: SAACL, <http://web.stanford.edu/group/sacl/home.html#>
 56. Maillard, T., Claeysen, F., LeLetty, R., Sosnicki, O., Pages, A., Carazo, A.V.: Piezomechatronic-based systems in aircraft, space, and defense applications. In: *Space Exploration Technologies II*. p. 73310K. International Society for Optics and Photonics (2009)
 57. Marutake, M.: The days when piezoelectric PVDF was discovered. *Ferroelectrics*. 171, 5–6 (1995)
 58. Bune, A. V, Zhu, C., Ducharme, S., Blinov, L.M., Fridkin, V.M., Palto, S.P., Petukhova, N.G., Yudin, S.G.: Piezoelectric and pyroelectric properties of ferroelectric Langmuir–Blodgett polymer films. *Journal of applied physics*. 85, 7869–7873 (1999)
 59. Bar-Cohen, Y., Xue, T., Lih, S.-S.: Polymer piezoelectric transducers for ultrasonic NDE. (1996)
 60. Furukawa, T.: Ferroelectric properties of vinylidene fluoride copolymers. *Phase Transitions: A Multinational Journal*. 18, 143–211 (1989)
 61. Vinogradov, A., Holloway, F.: Electro-mechanical properties of the piezoelectric polymer PVDF. *Ferroelectrics*. 226, 169–181 (1999)
 62. Ford, T.A., Edward, H.W.: Polyvinylidene fluoride and process for obtaining the same, (1948)
 63. Lovinger, A.J.: Poly (vinylidene fluoride), *Development in Crystalline Polymers*, DC Bassett, ed. Applied Science, London. 1, 26 (1982)
 64. Bar-Cohen, Y., Leary, S.P., Shahinpoor, M., Harrison, J.S., Smith, J.G.: Flexible low-mass devices and mechanisms actuated by electroactive polymers. In: *Smart Structures and Materials 1999: Electroactive Polymer Actuators and Devices*. pp. 51–57. International Society for Optics and Photonics (1999)
 65. Vinogradov, A.M., Holloway, F.: Dynamic mechanical testing of the creep and relaxation properties of polyvinylidene fluoride. *Polymer Testing*. 19, 131–142 (2000)
 66. Engel, M., Hisgen, B., Keller, R., Kreuder, W., Reck, B., Ringsdorf, H., Schmidt, H.-W., Tschirner, P.: Synthesis, structure and properties of liquid crystalline polymers. *Pure and Applied Chemistry*. 57, 1009–1014 (1985)
 67. Farmer, B.L., Hopfinger, A.J., Lando, J.B.: Polymorphism of poly (vinylidene fluoride): potential energy calculations of the effects of head-to-head units on the chain

- conformation and packing of poly (vinylidene fluoride). *Journal of Applied Physics*. 43, 4293–4303 (1972)
68. Mohamadi, S.: Preparation and characterization of PVDF/PMMA/graphene polymer blend nanocomposites by using ATR-FTIR technique. In: *Infrared Spectroscopy-Materials Science, Engineering and Technology*. IntechOpen (2012)
 69. Yang, X., Kong, X., Tan, S., Li, G., Ling, W., Zhou, E.: Spatially-confined crystallization of poly (vinylidene fluoride). *Polymer international*. 49, 1525–1528 (2000)
 70. Wise, D.L., Wnek, G.E., Trantolo, D.J., Cooper, T.M., Gresser, J.D.: *Photonic Polymer Systems: Fundamentals: Methods, and Applications*. CRC Press (1998)
 71. Haponska, M., Trojanowska, A., Nogalska, A., Jastrzab, R., Gumi, T., Tylkowski, B.: PVDF membrane morphology—influence of polymer molecular weight and preparation temperature. *Polymers*. 9, 718 (2017)
 72. Sajkiewicz, P., Wasiak, A., Gocłowski, Z.: Phase transitions during stretching of poly (vinylidene fluoride). *European polymer journal*. 35, 423–429 (1999)
 73. Hsu, C.C., Geil, P.H.: Morphology-structure-property relationships in ultraquenched poly (vinylidene fluoride). *Journal of applied physics*. 56, 2404–2411 (1984)
 74. Kepler, R.G., Anderson, R.A.: Ferroelectric polymers. *Advances in physics*. 41, 1–57 (1992)
 75. Gusarov, B.: PVDF piezoelectric polymers: characterization and application to thermal energy harvesting, (2015)
 76. Li, X., Tabil, L.G., Panigrahi, S.: Chemical treatments of natural fiber for use in natural fiber-reinforced composites: a review. *Journal of Polymers and the Environment*. 15, 25–33 (2007)
 77. Kensch, C.: Influence of composite fatigue properties on lifetime predictions of sailplanes. *Technical Soaring*. 19, 69–76
 78. DANTEC DYNAMICS: DIC Measurement Principle, <https://www.dantecdynamics.com/measurement-principles-of-dic>
 79. Orteu, J.-J.: 3-D computer vision in experimental mechanics. *Optics and lasers in engineering*. 47, 282–291 (2009)
 80. Ali-Ahmad, M., Subramaniam, K., Ghosn, M.: Experimental investigation and fracture analysis of debonding between concrete and FRP sheets. *Journal of engineering mechanics*. 132, 914–923 (2006)
 81. Tyson, J., Schmidt, T., Galanulis, K.: Advanced photogrammetry for robust deformation and strain measurement. In: *Proceedings of SEM 2002 annual conference, Milwaukee, WI* (2002)
 82. Lopez-Anido, R., El-Chiti, F.W., Muszyński, L., Dagher, H.J., Thompson, L., Hess, P.E.: Composite material testing using a 3-D digital image correlation system. *Composites*. 6–8 (2004)

83. Overview of Acoustic Emission Testing (AET), <https://inspectioneering.com/tag/acoustic+emission>
84. C. Visconti, I., Teti, R.: Acoustic emission from composite materials. (1979)
85. Center, N. resource: Introduction to Acoustic Emission Testing, [https://www.nde-ed.org/EducationResources/CommunityCollege/Other Methods/AE/AE_Intro.htm](https://www.nde-ed.org/EducationResources/CommunityCollege/Other%20Methods/AE/AE_Intro.htm)
86. Sachse, W., Yamaguchi, K., Roget, J.: Acoustic emission: current practice and future directions. Presented at the (1991)
87. Jensen, L.F., Hansen, M.M., Pertoldi, C., Holdensgaard, G., Mensberg, K.-L.D., Loeschcke, V.: Local adaptation in brown trout early life-history traits: implications for climate change adaptability. *Proceedings of the Royal Society B: Biological Sciences.* 275, 2859–2868 (2008)
88. Higo, Y., Inaba, H.: The general problems of AE sensors. In: *Acoustic Emission: Current practice and future directions.* ASTM International (1991)
89. Hellier, C.J.: Radiographic testing. *Handbook of Non-destructive Evaluation*, McGraw-Hill, New York, NY. (2001)
90. Unnþórsson, R.: Hit detection and determination in AE bursts. In: *Acoustic Emission-Research and Applications.* IntechOpen (2013)
91. Ramirez, G., Ziehl, P.H., Fowler, T.J.: Nondestructive evaluation of FRP design criteria with primary consideration to fatigue loading. *Journal of pressure vessel technology.* 126, 216–228 (2004)
92. Hamstad, M.A.: *Acoustic Emission Primer*, Lecture delivered by Dr. Hamstad at the acoustic emission working group meeting on august 4, 2003 (aewg-46). internet, 2004
93. Shull, P.J.: *Nondestructive evaluation: theory, techniques, and applications.* CRC press (2002)
94. Lakshmanan, M.K., Nikookar, H.: A review of wavelets for digital wireless communication. *Wireless Personal Communications.* 37, 387–420 (2006)
95. Prosser, W.H.: *Advanced AE techniques in composite materials research.* (1996)
96. Prosser, W.H.: *Waveform analysis of AE in composites.* (1998)
97. Tsamtsakis, D., Wevers, M., De Meester, P.: Acoustic emission from cfrp laminates during fatigue loading. *Journal of reinforced plastics and composites.* 17, 1185–1201 (1998)
98. Nayeb-Hashemi, H., Kasomino, P., Saniei, N.: Nondestructive evaluation of fiberglass reinforced plastic subjected to combined localized heat damage and fatigue damage using acoustic emission. *Journal of nondestructive evaluation.* 18, 127–137 (1999)
99. Kamala, G., Hashemi, J., Barhorst, A.A.: Discrete-wavelet analysis of acoustic emissions during fatigue loading of carbon fiber reinforced composites. *Journal of Reinforced Plastics and Composites.* 20, 222–238 (2001)

100. Bhat, M.R., Majeed, M.A., Murthy, C.R.L.: Characterization of fatigue damage in unidirectional GFRP composites through acoustic emission signal analysis. *NDT & E International*. 27, 27–32 (1994)
101. De Groot, P.J., Wijnen, P.A.M., Janssen, R.B.F.: Real-time frequency determination of acoustic emission for different fracture mechanisms in carbon/epoxy composites. *Composites Science and Technology*. 55, 405–412 (1995)
102. Seyyed Monfared Zanjani, J., Saner Okan, B., Letofsky-Papst, I., Yildiz, M., Menciloglu, Y.Z.: Rational design and direct fabrication of multi-walled hollow electrospun fibers with controllable structure and surface properties. *European Polymer Journal*. 62, 66–76 (2015). doi:<https://doi.org/10.1016/j.eurpolymj.2014.10.019>
103. Wan, X., Lu, H., Kang, J., Li, S., Yue, Y.: Preparation of graphene-glass fiber-resin composites and its electromagnetic shielding performance. *Composite Interfaces*. 25, 883–900 (2018). doi:[10.1080/09276440.2018.1439641](https://doi.org/10.1080/09276440.2018.1439641)
104. Manna, S., Batabyal, S.K., Nandi, A.K.: Preparation and characterization of silver– poly (vinylidene fluoride) nanocomposites: formation of piezoelectric polymorph of poly (vinylidene fluoride). *The Journal of Physical Chemistry B*. 110, 12318–12326 (2006)
105. Mago, G., Kalyon, D.M., Fisher, F.T.: Membranes of polyvinylidene fluoride and PVDF nanocomposites with carbon nanotubes via immersion precipitation. *Journal of Nanomaterials*. 2008, 17 (2008)
106. Parangusan, H., Ponnamma, D., Al-Maadeed, M.A.A.: Stretchable electrospun PVDF-HFP/Co-ZnO nanofibers as piezoelectric nanogenerators. *Scientific reports*. 8, 754 (2018)
107. Marques, R., Unel, M., Yildiz, M., Suleman, A.: Remaining useful life prediction of laminated composite materials using Thermoelastic Stress Analysis. *Composite Structures*. 210, 381–390 (2019). doi:<https://doi.org/10.1016/j.compstruct.2018.10.047>
108. Sherrit, S., Mukherjee, B.K.: The use of complex material constants to model the dynamic response of piezoelectric materials. In: 1998 IEEE Ultrasonics Symposium. Proceedings (Cat. No. 98CH36102). pp. 633–640. IEEE (1998)
109. Singh, D., Choudhary, A., Garg, A.: Flexible and Robust Piezoelectric Polymer Nanocomposites Based Energy Harvesters. *ACS Applied Materials & Interfaces*. 10, 2793–2800 (2018). doi:[10.1021/acsami.7b16973](https://doi.org/10.1021/acsami.7b16973)
110. Natarajan, V., Gangarao, H.V.S., Shekar, V.: Fatigue response of fabric-reinforced polymeric composites. *Journal of composite materials*. 39, 1541–1559 (2005)
111. Keulen, C.J., Akay, E., Melemez, F.F., Kocaman, E.S., Deniz, A., Yilmaz, C., Boz, T., Yildiz, M., Turkmen, H.S., Suleman, A.: Prediction of fatigue response of composite structures by monitoring the strain energy release rate with embedded fiber Bragg gratings. *Journal of Intelligent Material Systems and Structures*. 27, 17–27 (2016)
112. Jollivet, T., Peyrac, C., Lefebvre, F.: Damage of composite materials. *Procedia Engineering*. 66, 746–758 (2013)
113. Elsherbini, Y.M., Hoa, S. V: Experimental and numerical investigation of the effect of

gaps on fatigue behavior of unidirectional carbon/epoxy automated fiber placement laminates. *Journal of Composite Materials*. 51, 759–772 (2017)